

Copyright

by

Utkur Mirsaidov

2005

The Dissertation Committee for Utkur Mirsaidov
certifies that this is the approved version of the following dissertation:

**Nuclear Magnetic Resonance Force Microscopy of
Ammonium Dihydrogen Phosphate and Magnetism of
Cobalt Nanocrystals**

Committee:

John T. Markert, Supervisor

Chih-Kang Shih

Alejandro de Lozanne

Brian Korgel

Allan H. MacDonald

**Nuclear Magnetic Resonance Force Microscopy of
Ammonium Dihydrogen Phosphate and Magnetism of
Cobalt Nanocrystals**

by

Utkur Mirsaidov, B.S.

Dissertation

Presented to the Faculty of the Graduate School of

The University of Texas at Austin

in Partial Fulfillment

of the Requirements

for the Degree of

Doctor of Philosophy

The University of Texas at Austin

December 2005

Dedicated to my parents for their never ending love.

Acknowledgments

I am grateful to my loving mother for enduring all the hardship while bringing up me and my brother; for always being there for us. I am grateful to my dad for taking great care of his family, for providing the best education available to us, for always staying true to his principles through turbulent times.

I would like to thank John Markert, my supervisor, my teacher and a great friend. His patience has no boundaries, I am a living proof of that. Under his guidance I freed myself from very bad habits such as frequently breaking lab equipment, currently I only break things every once in a while. The freedom he granted me to pick my sample of study and to design my experiment with the available equipment was very important in developing my thought process. I learned that critically analyzing an experiment and calculating before setting things up is quite important. John is also a great mentor, his encouragements came when I needed them. Talking to John was always very enjoyable. Wherever life takes me from here, I will miss our daily conversations. I really do think that I am very different person than I was 5.5 years ago, primarily due to John and I am very grateful for that. Thanks for everything, John!!!

My next thanks goes to Dr. Miller, friend, colleague and drinking buddy. His enthusiasm in lab was a turning point in my life. Working with him was a valuable experience. He is the only man I know for whom being impatient pays off. His hands on approach to every problem showed me that sometimes, only sometimes,

it is just better to try things out instead of thinking them over and complicating things.

I would also like to thank my lab-mates: Yong Lee, for his helpful advice on electronics and other technical challenges. I can not imagine figuring out everything by myself. Without his advice and suggestions during my early years in the lab I would be lost. I also enjoyed working with Keeseong Park; his funny comments were very stimulating. In some sense he is like John, always thorough and focused on a project. I appreciate Wei Lu, Samaresh Guchhait and Rosie Cardenas for helping me out now and then, Han-Jong Chia who joined our group this summer was very helpful to me with ovens and proofreading this dissertation. Thank Y'all!!!

My floormates: Casey Israel is good colleague and friend, a real Texan with an open heart and a really nice friend. Weida Wu, a bright individual who knows something about everything in physics. Our occasional discussions about some topics in physics were always enlightening for me. And everyone in Alex de Lozanne's lab, Min, Changbae, Junwei and Jeehoon were always helpful. Theorist folks: Dimi, his everyday sarcasm made my life brighter. And of course Di without his help with LaTeX this dissertation would not be possible. I also want to thank Steve Li, from Dr. Shih's lab, he did a great job providing us with the cobalt nanocrystal samples discussed in Chapter 6 of this dissertation. Thank You All!!!

I would also like to thank Dr. Shih for his his occasional conversations on weekends that helped reset my mind and his collaboration on the nanocrystal project. I am also grateful to Alex de Lozanne for letting me steal coffee from his lab.

And of course, Jack Clifford, a very helpful individual. He is very famous, all the experimentalists know him. He will help you in anyway he can. Most projects here, in the Physics Department, would not be possible without his direct help. Thank you Jack for all your help and not getting extremely mad at me when I

pushed the Machine Shop safety rules to their limits.

I would like to thank Allan of Machine Shop, Ed and Lanny of Cryo Shop for their constant help.

I would also like to thank my friend Denis Potapov for everything he has done and will do for me. I am lucky to have a friend like him.

My everyday life outside of physics would be very boring without a special someone. Ann, thanks for loving and taking care of me and most importantly making me happy just by being there. You are one of the best things that ever has happened to me.

I am also extremely grateful to my countrymen whose hard earned money made it possible for me to to get my undergraduate degree here in the great state of Texas.

UTKUR MIRSAIDOV

The University of Texas at Austin

December 2005

Nuclear Magnetic Resonance Force Microscopy of Ammonium Dihydrogen Phosphate and Magnetism of Cobalt Nanocrystals

Publication No. _____

Utkur Mirsaidov, Ph.D.

The University of Texas at Austin, 2005

Supervisor: John T. Markert

A Nuclear Magnetic Resonance Force Microscopy (NMR-FM) technique utilizing a somewhat uncommon experimental geometry has been developed.

Characterization of external field effects on soft permalloy micromagnets on double torsional oscillators was performed. We showed that at high enough fields (above 1 Tesla), the quality factor for each mode is comparable to the zero field value. The changes in resonance frequency fit well with our model, and permitted high-sensitivity magnetic moment and magnetic anisotropy measurement.

Effects of laser power on cantilevers used for NMR-FM has been studied in

detail. The origins of the observed self-sustained oscillations has been addressed by our model.

NMR-FM detection has been shown in an ammonium dihydrogen phosphate sample. Imaging and spin manipulation techniques were used for the first time to detect the nuclear spins in a sample with short relaxation times.

A magnetic study of epitaxially grown cobalt nanocrystals on a Si(111) substrate has been performed. Enhancement of the magnetic moment and anisotropy energy have been observed and data are consistent with single domain model. Experimental evidence indicates small inter-nanocrystal interactions.

Finally, future directions in achieving the single-spin detection limit is addressed.

Contents

Acknowledgments	v
Abstract	viii
List of Tables	xiii
List of Figures	xiv
Chapter 1 An Overview of Nuclear Magnetic Resonance Force Mi-	
croscopy	1
1.1 Conventional Nuclear Magnetic Resonance	1
1.2 Principles of Magnetic Resonance Force Microscopy	5
Chapter 2 Experimental Setup and Considerations for Nuclear Mag-	
netic Resonance Force Microscopy	12
2.1 General Overview of the NMRFM Probe	12
2.2 Micro-Oscillators for NMRFM	14
2.3 Fiber Interferometer	18
2.4 Feedback	21
2.5 Careful Lock-In Detection	23
2.6 Multi-functional Piezo Scanner and Coarse Approach	24
2.7 Permanent Magnet	28

2.8	RF Coil and Tuning Capacitors	31
2.9	RF Modulation Electronics	32
2.10	Technical Challenges	36
Chapter 3 Cavity Induced Self-Sustained Oscillations of Micro Cantilevers		41
3.1	Brief Overview of Self Oscillations	41
3.2	Self oscillation of a Single Crystal Silicon Cantilever	44
Chapter 4 Effects of External Field on Torsional Oscillators with Micromagnets		51
Chapter 5 Results and Discussion		60
5.1	Experimental Parameters	60
5.2	Detection of the NMRFM signal from ADP sample	61
5.3	Characterization	64
5.4	Spin Manipulation with Pulses	67
Chapter 6 Magnetism In Cobalt Nanocrystals		69
6.1	Motivation	69
6.2	Sample Preparation	70
6.3	Magnetic Measurement and Analysis	72
6.4	Is Single Nuclear Spin Detection Possible?	77
Appendix		78
Appendix A Operating The Set-up		79
A.1	Electromagnet	79
Bibliography		82

List of Tables

4.1	The resonance frequencies and quality factors of four major oscillation modes of our two double torsional oscillators (see text for more information).	52
5.1	The experimental parameters used for imaging the ADP sample. . .	61
5.2	Experimental parameters.	64
5.3	Adiabatic factor versus FM RF field. Amplitude of the modulation is 280 kHz.	67
5.4	Experimental parameters.	67

List of Figures

1.1	RF pulse applied at $t = 0$ along x' rotates the magnetization \mathbf{M}_0 to an angle $\theta = \gamma B_1 t$ in the $y' - z$ plane.	2
1.2	The effective field is slowly ramped down from the equilibrium value down to the resonance. This kind of slow ramp can lock the magnetization to the effective field.	3
1.3	Setup for conventional coil NMR. The oscillating RF field is applied perpendicular to the external polarizing field. Only the counterclockwise component of the RF field is used to manipulate the magnetization.	4
1.4	Common experimental configuration for Magnetic Resonance Force Microscopy.	6
1.5	Modulation sequence of the RF frequency. The RF frequency starts decaying to the resonance condition $\omega_{rf} = \omega_0$ from a reasonably large offset, and then frequency modulation was performed at the cantilever's resonant frequency, ω_{osc} with modulation amplitude of Ω	8
1.6	Cyclic adiabatic inversion of the magnetization in the rotating frame. The modulated z component of the effective field gives rise to the oscillating magnetization in the z direction.	9
1.7	Experimental configuration used in this work.	11
2.1	Image of the tip of the Probe	13

2.2	Bar Cantilever	14
2.3	a) Batch of paddle cantilevers, b) and c) are double torsional oscillators (Courtesy of Michelle Chabot)	16
2.4	Frequency sweep of the double torsional cantilever showing for different modes.	18
2.5	Phase sensitive detection showing lower cantilever and upper (antisymmetric) torsional mode with the measurements done at three points of the cantilever. X (blue dashed line), Y (red solid line) indicate that oscillation at point A, B and C are in phase for lower cantilever. X and Y are in phase for points A and C and out of phase with B for upper torsional mode.	19
2.6	Outline of the interferometer system.	20
2.7	Photodiode circuit for Fiber Interferometer.	20
2.8	Interference pattern measured by a photodiode, usually referred as the DC level. Distance between two peaks is a half wavelength of a 678 nm laser diode.	22
2.9	Feedback circuit to maintain oscillator to fiber end distance constant.	23
2.10	a) The driven scan of the cantilever with $f_0 = 1230$ Hz and $Q = 830$ fitted with a Lorentzian curve. b) The lock-in measurement of the driven scan with time constants of 10 ms, 30 ms, 100 ms, 300 ms, 1 s from bottom to top respectively.	25
2.11	Coarse z approach system with xyz scanning capabilities.	26
2.12	a) DC supply and b) amplifier for Tube Piezo.	27
2.13	Photodiode voltage versus number of sawtooth steps applied to move the stage with roughly ~ 1 gram of additional weight down (solid squares) and up (open circles) clearly reveals the reliable motion of the stage in z direction.	28

2.14	Magnetized iron sphere.	29
2.15	Component of the field along $-y$ direction (top) and its gradient in the z direction (bottom) versus the distance from the surface of the magnet in the z direction $(0, 0, d)$ induced by an iron sphere 2 mm in diameter.	30
2.16	Outline of the RF coil and tuning circuit.	32
2.17	Outline of the RF modulation electronics. All the switches in the diagram are shown in the triggered position.	33
2.18	Output of the pulse programmer (black curves) and modulation box (red curves). RF off corresponds to zero power output. a) Modulation sequence widely used in imaging. b) Sequence used for spin nutation and for T_1 measurement.	35
2.19	SEM image of the double torsional oscillator coated with Y and Pd metals. The image shows how a masking problem resulted in the film coating the lower neck of the oscillator.	37
2.20	SEM image of the melted ammonium dihydrogen phosphate (ADP) covering the entire head of the double torsional oscillator.	38
2.21	SEM image of the ADP glued to the double torsional oscillator.	39
2.22	Change in the resonance frequency of the cantilever due to the RF power sent to the coil. The frequency modulated RF power pulses were sent to the coil for 500 ms with 10 seconds repetition time.	40
3.1	a) Image of the experimental setup and b) an SEM image of the paddle cantilever used in this study.	44
3.2	a) Normalized intensity versus cantilever-fiber distance measured with the photodiode. Letters B and R stand for blue and red detuning respectively. The driven scans obtained at b) 40 and c) 750 μW	45

3.3	Resonance frequency (top) and Brownian amplitude (bottom left) versus the laser power incident on the cantilever for both red detuning (squares) and blue detuning (circles). Some of the Brownian curves obtained for red detuning of the cavity.	47
3.4	a) Interference fringe obtained by ramping the cavity width along with the displacement of the cantilever for b) $240 \mu\text{W}$, c) $300 \mu\text{W}$, d) $390 \mu\text{W}$, e) $960 \mu\text{W}$. f) Fourier Transform of the noise obtained at the red detuning of the cavity. Note the many orders of magnitude of the ordinary.	49
4.1	Double -torsional micro-oscillators used in the micromagnetometry experiments. Oscillator A on top has a larger magnet ($15\mu\text{m} \times 15\mu\text{m} \times 30\text{nm}$). Oscillator B at the bottom has the smaller magnet ($3 \mu\text{m}$ -diameter, 180-nm -thick).	53
4.2	The major oscillation modes of our double torsional oscillators, and the geometry used to determine the magnetic energy and equilibrium moment directions. a)The lower cantilever mode. b)The lower torsional mode. c)The upper cantilever mode. d)The upper torsional mode.	54
4.3	Magnetic-field dependent resonant frequencies relative to the zero-field value for oscillator A (large magnet, left panel) and Oscillator B (small magnet, right panel). In each case the modes are: lower cantilever (upward triangles), lower torsional (downward triangles), upper cantilever (squares) and upper torsional (open circles).	56
4.4	Fits to the low-field and high-field regimes of the field-dependent mechanical oscillator resonant frequency, using Eqs. 4.4 and 4.5.	58

4.5	Quality factor as a function of field for the lower cantilever mode of Oscillator A (triangles) and Oscillator B (circles). Lines are guides to the eye.	59
5.1	$T_{1\rho}$ data for ADP in the vicinity of room temperature shown for both unannealed (open circles) and annealed samples (closed circles). The triangles indicate the T_1 values, which do not depend on annealing. Ref. [35].	61
5.2	Magnitude of the cantilever's response for NMRFM experiment. The cyclic inversion time is 300 ms and the lock-in time constant is 100 ms. The shown curve displays the magnitude of the measured signal with the background spurious excitation subtracted, and is an average of four measurements. This measurement produced the data point at $B_0 = 15100$ G for the 53.7 MHz curve in Figure 5.3.	62
5.3	Peak amplitude of cantilever response versus field for two different carrier frequencies seperated by 1 MHz. Each point represents an average of four measurements.	63
5.4	The vibration amplitude of the oscillator with the ADP for 19 Gauss (■), 15 Gauss (●), 10 Gauss (▲) versus frequency modulation amplitude. All the measurements were done on resonance. Each data point represents the average of 16 cyclic inversion measurements. . .	65
5.5	Cyclic inversion with RF field of a) 15 Gauss, b) 11 Gauss, c) 9 Gauss and d) 7 Gauss and the amplitude of FM is 280 kHz Duration of the inversion is 1.2 s, start and end times are indicated by the arrow. Each of these graphs is the result of 16 averagings.	66
5.6	Spin nutation data obtained by varying pulse width and sampling the magnetization for 600 ms with the cyclic inversion scheme. The wait time between the pulse and the sampling is 15 ms.	68

6.1	120×120nm ² STM image of self assembled equilateral Cobalt nanocrystals with the side dimensions of 5.5 nm and a 2ML height on top of Si (111). Inset shows an enlarged image of one of these Cobalt nanoplatelets. Tiny clusters in the inset are Al templates of 6 atoms each occupying half of the 7 x 7 unit cell.	71
6.2	Hysteresis curves for a sample with 50 percent aerial coverage obtained at 5 and 70 K with the field applied perpendicular to the surface of the substrate. Inset shows an enlarged image of the hysteresis curve.	73
6.3	(a) and (b) are the remnant moments of the systems with 25% and 15% areal coverage. (c) and (d) are the coercive fields of the systems with 25% and 15% areal coverage. For both samples superparamagnetic behavior sets in above 100 K. Dashed lines are guides for the eyes. (e) and (f) represent hysteresis curves fitted to the single domain model for a sample with 25% coverage at 200 K and 70 K (solid lines) above the blocking temperature, T_B . See the text for details. .	74
6.4	Field (left) and field gradient (right) along the easy axis of magnetization versus the distance from the surface of the nanocrystal.	77
A.1	Electromagnet	80

Chapter 1

An Overview of Nuclear Magnetic Resonance Force Microscopy

In this chapter the basic concepts of nuclear magnetic resonance (NMR) along with the motivation leading to force detected NMR and its concepts will be introduced.

1.1 Conventional Nuclear Magnetic Resonance

It is useful to review the basic concepts of Nuclear Magnetic Resonance before we proceed to Force Detected NMR.

The time evolution of a nuclear magnetic moment $\vec{\mu} = \gamma\mathbf{J} = \gamma\hbar\mathbf{I}$ placed in a magnetic field \mathbf{B}_0 applied along the z direction is determined by the torque $\vec{\mu} \times \mathbf{B}_0$ that leads to a change in angular momentum. The equation of motion then becomes

$$\frac{d\vec{\mu}}{dt} = \gamma\vec{\mu} \times \mathbf{B}_0 \quad (1.1)$$

According to this equation the nuclear spins will precess around \mathbf{B}_0 with an angular velocity of $\omega_0 = \gamma B_0$, known as the Larmor frequency. Now if we apply a RF field that is rotating in the $x - y$ plane with an angular frequency ω_{rf} in the same direction as the precession of the nuclear moment:

$$\mathbf{B}_1 = B_1(\cos(\omega_{rf}t)\hat{\mathbf{x}} + \sin(\omega_{rf}t)\hat{\mathbf{y}}) \quad (1.2)$$

and transform our equation of motion 1.1 from the laboratory frame, (x, y, z) , to the rotating frame, (x', y', z) , where \mathbf{B}_1 is static then the dynamics of the nuclear spins will be governed by:

$$\begin{aligned} \frac{d\vec{\mu}}{dt} &= \gamma\vec{\mu} \times \mathbf{B}_{\text{eff}} \\ \mathbf{B}_{\text{eff}} &= (B_0 - \frac{\omega_{rf}}{\gamma})\hat{\mathbf{z}} + B_1\hat{\mathbf{x}}' \end{aligned} \quad (1.3)$$

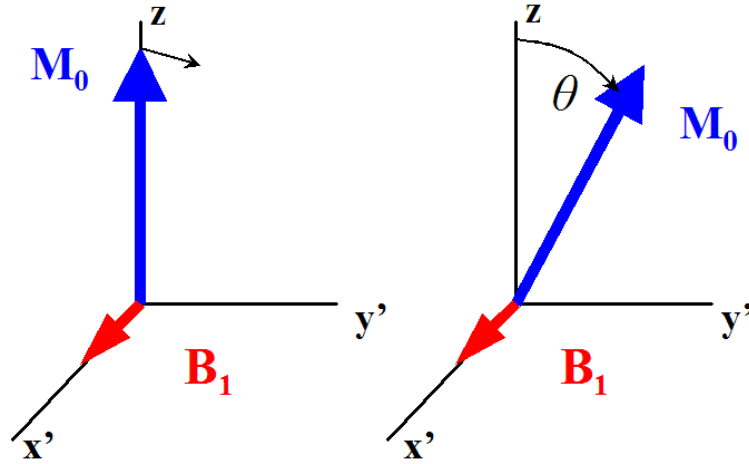


Figure 1.1: RF pulse applied at $t = 0$ along x' rotates the magnetization \mathbf{M}_0 to an angle $\theta = \gamma B_1 t$ in the $y' - z$ plane.

By manipulating the effective field seen by the nuclear spins we can control the dynamics of the magnetic moment in the rotating frame. A sudden pulse applied

for time t at the *resonance* condition, $\omega_{r,f} = \omega_0 = \gamma B_0$, will exert a torque $\vec{\mu} \times \mathbf{B}_1$ and will rotate the magnetic moment away from z in $y' - z$ plane as shown in Figure 1.1. The angle of rotation is $\theta = (\gamma B_1)t$. This sort of manipulation of the nuclear spins is the fundamental basis for all pulsed NMR techniques.

Another important way of manipulating the nuclear magnetization that is used to sample the nuclear spins in the NMRFM experiments is to vary \mathbf{B}_{eff} slowly so that the nuclear magnetization can follow the effective field given in Equation 1.3. When the RF field is off, the net magnetization is along the z axis, but once the field is turned on, we can slowly change the RF frequency to sweep \mathbf{B}_{eff} from the z direction to the direction of \mathbf{B}_1 . It is very important to start \mathbf{B}_{eff} almost parallel to \mathbf{B}_0 so that we can lock most of the spins to the effective field at the beginning of this *adiabatic inversion*. An illustration of the slow adiabatic passage of the nuclear spins is shown in Figure 1.2.

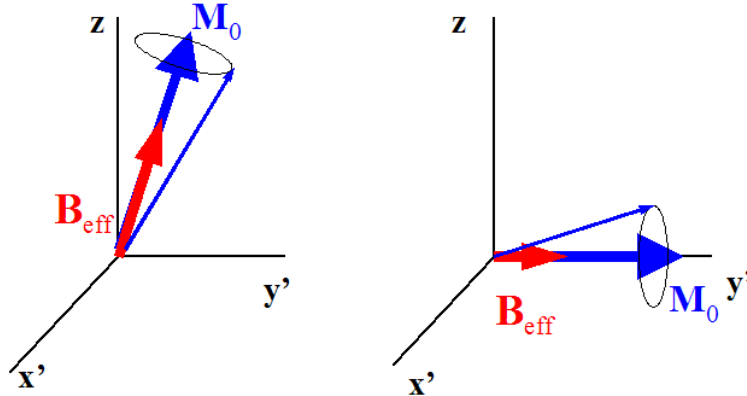


Figure 1.2: The effective field is slowly ramped down from the equilibrium value down to the resonance. This kind of slow ramp can lock the magnetization to the effective field.

The setup for conventional NMR is fairly simple. A sample is placed within a coil that produces a linearly oscillating RF field perpendicular to the external field \mathbf{B}_0 , let's say in x direction, $\mathbf{B}_1 = 2B_1 \cos(\omega_{r,f}t)\hat{x}$ (see Figure 1.3). This field can be

decomposed into two components, clockwise and counterclockwise rotating fields. A field rotating against the precession will not affect the nuclear motion because on resonance it will have twice the Larmor frequency.

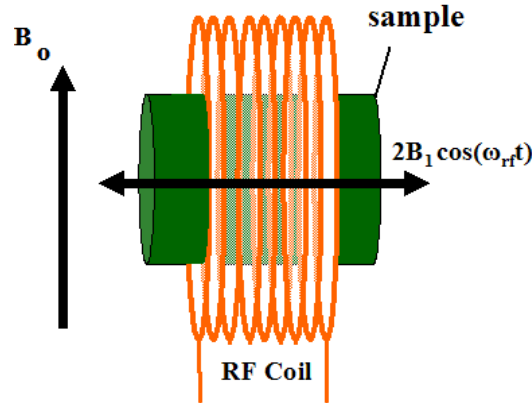


Figure 1.3: Setup for conventional coil NMR. The oscillating RF field is applied perpendicular to the external polarizing field. Only the counterclockwise component of the RF field is used to manipulate the magnetization.

The same coil can be used to detect nuclear magnetic resonance. The coil is sensitive to changes in magnetization in the $x' - y'$ plane.

The thermal relaxation of the nuclear moments after they have been disturbed from equilibrium is the measure of the coupling of the nuclei to its environment. The relaxation process is determined by how efficiently nuclei can give out their energy to their surroundings via electromagnetic interactions. The characteristic time scale is called spin-lattice or longitudinal relaxation time and denoted by T_1 . So when the disturbed magnetization returns back to the equilibrium to point along the external polarizing field the transverse component of the NMR signal disappears.

Another interesting time scale for NMR experiments is spin-spin or transverse relaxation time T_2 . The accurate measurement of this time scale informs us on the

local environment of the nuclei, since depending on the field seen by nuclei they will precess at different angular velocities thus dephasing in the $x - y$ plane.

Armed with the basic knowledge of spin manipulation we are ready to start the discussion of force detected NMR.

1.2 Principles of Magnetic Resonance Force Microscopy

Since the first successful NMR was detected in 1946 the technique has improved extraordinarily. Switching to microcoils allowed somewhat high resolution Magnetic Resonance Imaging (MRI). However, the limitations of the inductive detection technique do not permit measurement of NMR at the microscale. In 1991 John Sidles proposed a new way of detecting signals from resonating nuclear and electron spins. The proposed technique involved coupling the nuclear moment to a micromechanical resonator and detecting the NMR mechanically to attain high sensitivity. In 1994 an IBM group led by Dan Rugar demonstrated the first force detection of nuclear spins in an ammonium sulphate sample [2]. 10 years later the same group successfully detected a single electron spin [3].

The basic principle of mechanical detection of Nuclear Magnetic Resonance can be realized through the setup shown in Figure 1.4.

Placing the sample in the external field \mathbf{B}_0 will result in a net magnetization along the applied field. The gradient from a micromagnet on the mechanical oscillator will couple to the magnetization of the sample. Then, using the RF field, we can start modulating the magnetization in a thin *resonance* slice of the sample at the cantilever's resonance frequency, which in turn will result in an oscillation of the magnetic force, with amplitude F , at the frequency that will ring up the cantilever. The vibration amplitude of the resonator,

$$A = \frac{FQ}{k} \tag{1.4}$$

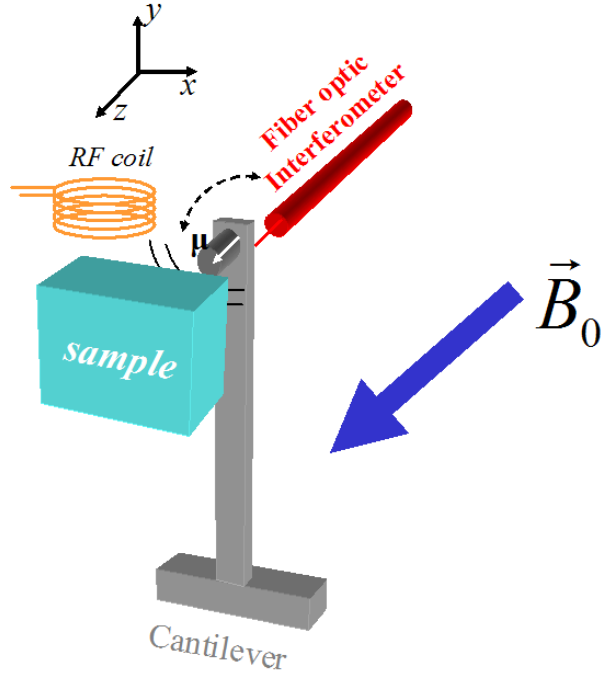


Figure 1.4: Common experimental configuration for Magnetic Resonance Force Microscopy.

is then detected by a fiber optic interferometer. Here Q and k are the quality factor and the spring constant of the cantilever, respectively.

Before going into the details of how the resonance slice and the modulation of the magnetization in that slice is achieved, we should point out the advantages of force detected NMR over conventional NMR.

The Signal to Noise Ratio (SNR) of conventional NMR is given by [6]:

$$SNR = \frac{N\gamma^3\hbar^2 B_0^2 I(I+1)}{3k_B T} \sqrt{\frac{\mu_0 Q}{4k_B T \Delta\nu V_{coil}}} \quad (1.5)$$

Here Q is the quality factor of the receiver circuit that consists of coil, capacitor and resistor¹, V_{coil} is the volume of the coil that is filled with the sample, B_0 is

¹Resistance is introduced due to the wiring of the circuit.

the polarizing external field, T is the temperature of the system. γ , \hbar and k_B are the gyromagnetic ratio of the nuclei, Plank's constant and Boltzmann's constant, respectively.

For mechanical detection, the thermal noise of the cantilever

$$F_{min} = \sqrt{\frac{4kk_B T \Delta\nu}{Q\omega_{osc}}} \quad (1.6)$$

will be the main limiting factor for measurement of the magnetic force experienced by the cantilever, $\mathbf{F} = (\boldsymbol{\mu} \cdot \nabla)\mathbf{B}$, the SNR can be written as [5]

$$SNR = \frac{N\gamma^2\hbar^2(\nabla B)B_0I(I+1)}{3k_B T} \sqrt{\frac{Q\omega_{osc}}{4kk_B T \Delta\nu}} \quad (1.7)$$

Notice here that in conventional NMR, the SNR goes as the square of the polarizing field and for NMRFM the relation between field and sensitivity is linear. This removes the strong necessity of having large fields. Improvement in SNR for mechanical cantilevers can be greatly enhanced by increasing the field gradient and using soft cantilevers which are easily achievable by today's MEMS fabrication techniques [6].

Now, we can expand upon the details of how mechanical detection of NMR can be achieved with a cantilever. The first demonstration of force detected NMR used a very simple spin manipulation technique that has also been utilized in my work. The RF was swept from far above resonance to the resonance frequency, $\omega_{rf} = \omega_0 = \gamma B_0$, and then a sinusoidal modulation of RF was performed. The output of the modulation electronics is shown in Figure 1.5.

The reason for starting the frequency sweep far away from resonance is to ensure that B_{eff} is aligned with the net magnetization of the sample so that maximum locking of the magnetic moment to the effective field is achieved, as mentioned in the previous section. Once the spins are brought to the Larmor resonance condition,

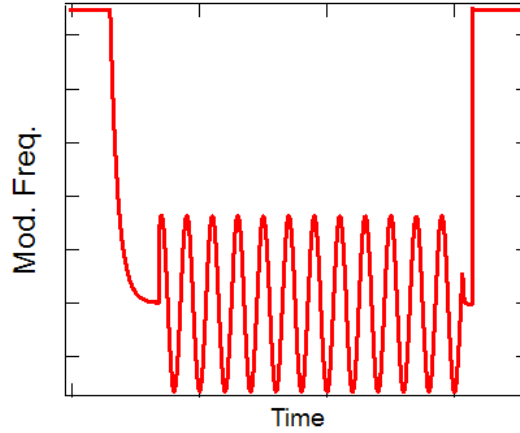


Figure 1.5: Modulation sequence of the RF frequency. The RF frequency starts decaying to the resonance condition $\omega_{rf} = \omega_0$ from a reasonably large offset, and then frequency modulation was performed at the cantilever's resonant frequency, ω_{osc} with modulation amplitude of Ω .

frequency modulation of the RF at the cantilever's resonant frequency, ω_{osc} , with a frequency modulation amplitude Ω is initiated. The modulated frequency

$$\omega_{rf} = \omega_0 + \Omega \sin(\omega_{osc}t) \quad (1.8)$$

will produce the effective field with the oscillating z component,

$$\mathbf{B}_{\text{eff}} = \frac{\Omega \sin(\omega_{osc}t)}{\gamma} \hat{z} + B_1 \hat{x}' \quad (1.9)$$

at the cantilever's resonance frequency. The illustration shown in Figure 1.6 provides a good description of what happens during the modulation. The net nuclear magnetization will lock to the effective field and precess around it, while the z component of the magnetization is sinusoidally modulated according to 1.3:

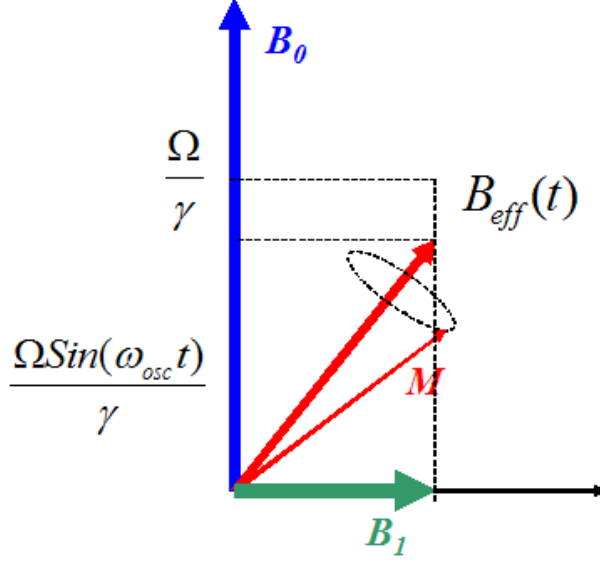


Figure 1.6: Cyclic adiabatic inversion of the magnetization in the rotating frame. The modulated z component of the effective field gives rise to the oscillating magnetization in the z direction.

$$\mu_z(t) = -\mu_0 \frac{(\Omega/\gamma) \sin(\omega_{osc}t)}{\sqrt{(\Omega/\gamma)^2 \sin^2(\omega_{osc}t) + B_1^2}} \quad (1.10)$$

The presence of the field gradient makes it possible for only the nuclear moments inside the field interval,

$$\Delta B = \frac{\Delta\omega}{\gamma} = \frac{2\Omega}{\gamma} \quad (1.11)$$

centered at B_0 to undergo the oscillations. The resonance slice is then defined as the region where the resonance condition is met:

$$\Delta z = \frac{2\Omega/\gamma}{\nabla_z B} \quad (1.12)$$

Thus the modulated force experienced by the cantilever, $F_z(t) = \mu_z(t)\nabla_z B$, is the basis of mechanical detection of NMR.

So far we have assumed that the change in the effective field was done slowly enough to satisfy the adiabatic inversion condition. This condition states that at any time the change in the effective field must be much slower than the precession of the magnetic moment around that field. Setting the minimum value of the angular velocity of the precession, γB_1 , much larger than the maximum angular velocity of the effective field, $d\phi/dt|_{max}$, will guarantee that this condition is satisfied during the modulation. If we consider the tangent the angle ϕ that the effective field makes with the x axis,

$$\tan \phi = \frac{(\Omega/\gamma) \sin(\omega_{osc}t)}{\sqrt{(\Omega/\gamma)^2 \sin^2(\omega_{osc}t) + B_1^2}} \quad (1.13)$$

the angular velocity of the effective field can be obtained by simply taking the derivative of this expression and solving the result for $d\phi/dt$. The largest value of the angular velocity is achieved when B_{eff} is along B_1 and equal to $d\phi/dt|_{max} = (\omega_{osc}\Omega)/(\gamma B_1)$. The adiabatic condition for cyclic inversion, $d\phi/dt|_{max} \ll \gamma B_1$ can be written as:

$$\frac{(\gamma B_1)^2}{\omega_{osc}\Omega} \gg 1 \quad (1.14)$$

Before concluding this section it is advantageous to describe the setup used for this particular work, shown in Figure 1.7, and to describe how the same principles apply for this experimental geometry. This experimental setup is very similar to the one used for the first mechanical detection of electron spin resonance [7].

The external field applied along the y direction induces the magnetization of the sample to align in the same direction. The z component of the magnetic force that is needed to excite the cantilever is $F_z(t) = \mu_y(t)dB_y/dz = \mu_y(t)dB_z/dy$. The details of the field and field gradient generated by the spherical magnet will be discussed later in Section 2.7.

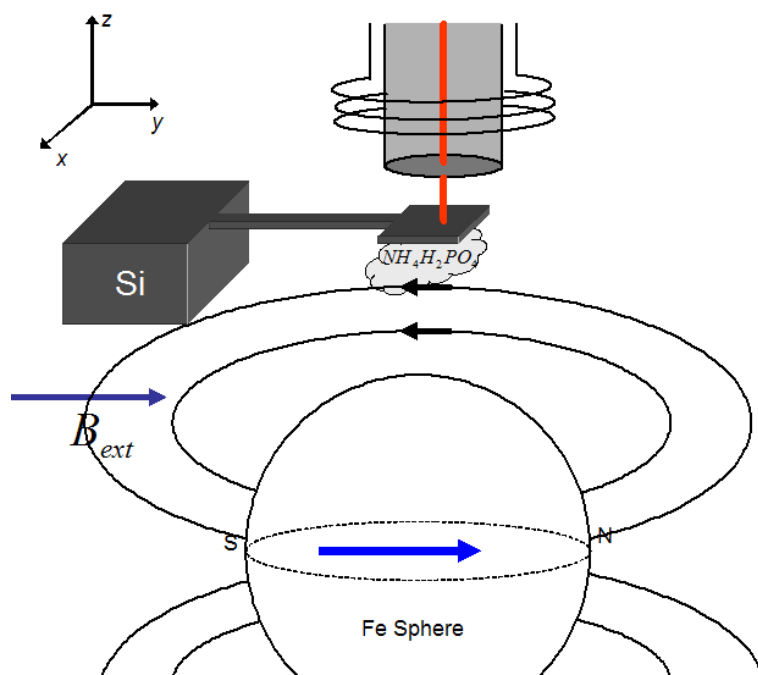


Figure 1.7: Experimental configuration used in this work.

Chapter 2

Experimental Setup and Considerations for Nuclear Magnetic Resonance Force Microscopy

This chapter will give an overview of the setup I have used for the NMRFM experiment.

2.1 General Overview of the NMRFM Probe

As was illustrated in Figure 1.7, the general MRFM probe consists of an RF coil, a gradient-producing permanent magnet, a cantilever, and a fiber interferometer to detect the motion of the cantilever. Figure. 2.1 shows the probe used for the current experiment.

The fiber is securely attached to the fiber stage which can be moved up to 10 μm by a feedback piezo; the fiber passes through the RF coil without touching it.

The coarse mechanical approach system that is used for manually moving the fiber stage for approach (not shown here) helps to bring the fiber close to the cantilever. The fiber is aligned to the oscillator by adjusting a positioning screw on the oscillator stage and by the manual fiber approach. The separation between fiber end and the oscillator is typically 20 to 50 μm . The RF coil is placed 0.5 mm away from the cantilever with the sample. In order to achieve maximum transmission of the RF power we need to match the impedance between the output of the RF amplifier and RF input of the probe. This matching is achieved by tuning capacitors. The piezo tube scanner, which positions the small gradient-generating permanent magnet, has both capabilities of coarse approach and scanning. The pressure inside the probe is maintained around 10^{-4} torr.

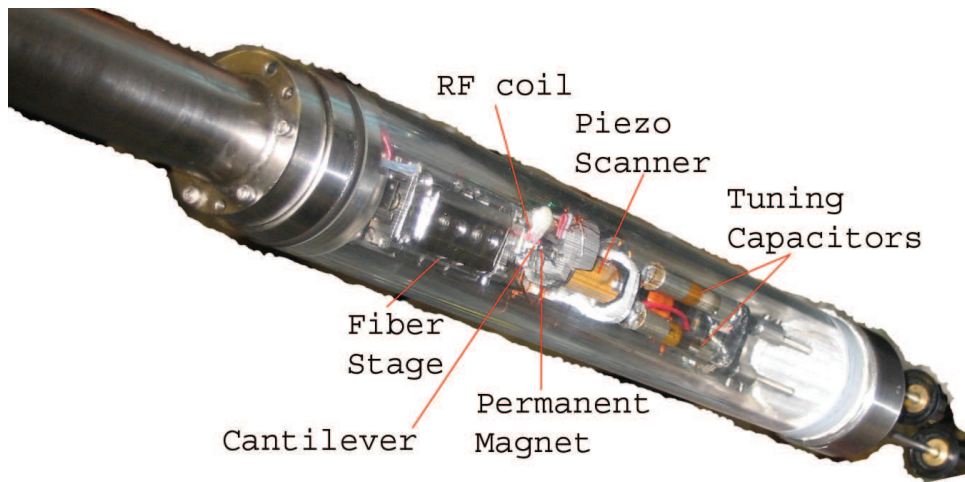


Figure 2.1: Image of the tip of the Probe

2.2 Micro-Oscillators for NMRFM

Micro oscillators are the essential part of MRFM because their sensitivity determines the sensitivity of the entire detection technique. As we saw in Section 1.2, to achieve high sensitivities in the presence of thermal noise we will need a cantilever with a high Q and a low spring constant, k . It is also important to maintain the resonance frequency of the cantilever such that it does not violate the adiabatic condition discussed in Section 1.2. Single crystal silicon wafers are used to manufacture micro oscillators with low internal friction to achieve high Q values. Scanning Electron Microscope (SEM) images of some paddle cantilever and double torsional oscillator designs are illustrated in Figure 2.3.

The spring constant of the bar cantilever shown in Figure 2.2 is given by:

$$k = \frac{Et^3w}{4l^3} \quad (2.1)$$

where E , t , w and l are Young's modulus for silicon, thickness, width and length of the cantilever, respectively. One can reduce the spring constant through thinning

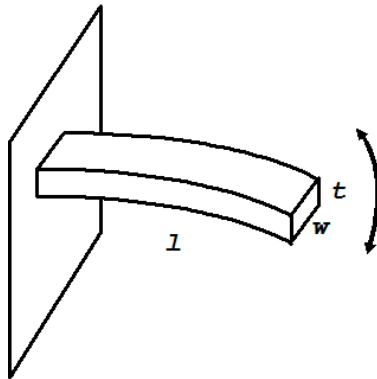


Figure 2.2: Bar Cantilever

and elongating the cantilevers; however, that makes them more prone to damage. Being fragile is not the only problem with low k cantilevers. The simple expression

for the rms position fluctuations of the mechanical cantilever due to thermal noise is

$$k \langle x^2 \rangle = k_B T \quad (2.2)$$

A low spring constant will give greater rms fluctuations, which will be a problem for higher resolutions. The current proposal and demonstrated solution for this problem is to use an active feedback. The idea is pretty straight forward. One needs to monitor the thermal fluctuations of the cantilever with the fiber interferometer and use a notch filter to apply negative feedback to the oscillation at the resonance frequency of the cantilever. However, before utilizing the active feedback it is extremely important to reduce the interferometer noise. We do not want to feed back laser noise into the cantilever. The negative feedback signal with the appropriate gain can be fed back into the cantilever by various mechanisms. The proposed method by John Sidles utilizes a separate coil providing a magnetic field as feedback that will interact with the micro magnet on the cantilever [8], [9], [10]. Another way to damp cantilever motion would be to coat the fiber with gold and provide an active feedback voltage, and therefore an electrostatic potential, that will interact with the cantilever. To reduce the the thermal fluctuations of the cantilevers further, John Markert has recently proposed using a Scanning Tunneling Microscope (STM) tip to measure tunneling current between the cantilever and a STM tip held close to the cantilever. Using the tunneling current as a measure of noise fluctuation is very reliable due to its sensitivity. Thus a reduction of spring constant requires a careful approach for high resolution imaging.

Now, what about increasing the quality factor of the cantilever? Once the cantilever is placed in a reasonable vacuum, 10^{-4} torr, the quality factor of the single crystal cantilevers is limited by the internal friction caused by defects in the crystal structure. At low temperatures some of these defects can be frozen thus resulting in a significant increase in the quality factor. One might choose to use a stiffer and

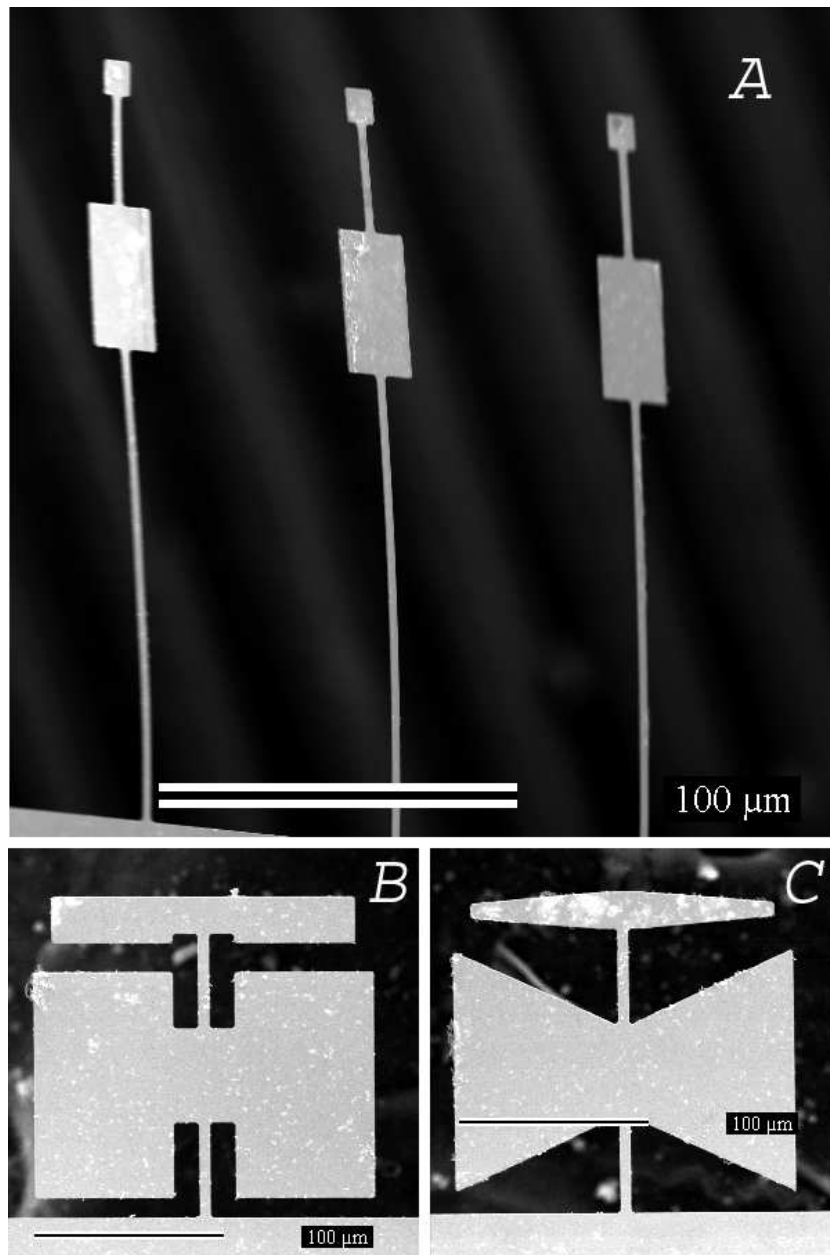


Figure 2.3: a) Batch of paddle cantilevers, b) and c) are double torsional oscillators (Courtesy of Michelle Chabot)

more robust cantilever with high Q value. It has been shown that the upper torsional mode of a carefully designed double torsional oscillator has superior Q value due to the confinement of the mechanical energy in the oscillator to the motion of the head [11], [12]. The antisymmetric twist of the light head and heavy wing of such an oscillator will limit the main motion to the head (this can be shown from the equation of motion or more simply argued to be due to the conservation of angular momentum), thus effectively decoupling the oscillations from the base. This in turn will shut down the energy leak from the oscillator. So the immediate advantage of robust torsional oscillators is small noise fluctuations that come with stiffness and high sensitivity. While high- Q oscillators have sensitivity advantages, there are disadvantages. High Q oscillators will take $Q/(\pi f_0)$ seconds for an appreciable ring up of the oscillator. If the time scale for the ring up becomes comparable to, or in a worst case scenario if it exceeds, the spin-lattice relaxation time, T_1 , then a sensible measurement of the signal will be complicated but still achievable through careful deconvolution of the magnetization signal from the time dependent measured signal. Another drawback of a high Q value is that frequency drifts, associated with the heating of the oscillator due to the RF power, will make it hard to stay on resonance during the measurement. This problem can be minimized by using micro scale RF coils that apply an almost local RF field thus reducing the thermal heating of the oscillator.

Driven frequency sweeps for one of our double torsional oscillators are shown in Figure 2.4. This plot shows peaks at the resonant frequencies of the four oscillation modes: lower cantilever, lower torsional, upper cantilever and upper torsional. Usually these oscillators have other modes as well. Phase sensitive detection (Figure 2.5) is used to differentiate between the different modes of oscillation. We can use the fiber optic interferometer to detect the motion of various parts of the oscillator, and by comparing the phase difference between the moving parts we can distinguish

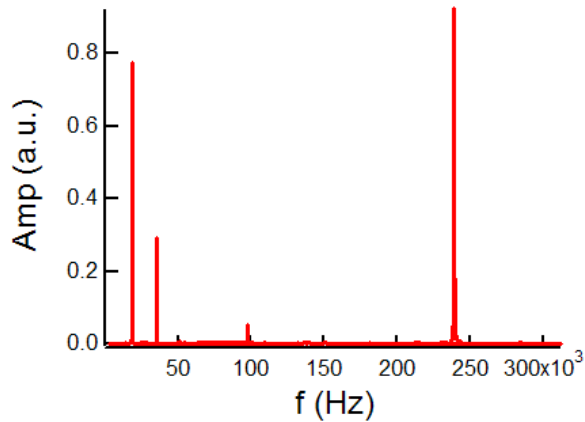


Figure 2.4: Frequency sweep of the double torsional cantilever showing for different modes.

the oscillation modes. To take full advantage of the high Q upper torsional mode, softer oscillators with low (< 20 kHz) upper torsional resonant frequency must be designed. Sinusoidal modulation of the nuclear magnetization at high frequency will result in poor spin locking (violation of the adiabatic condition) and will cause degradation of the detected signal as discussed in Section 1.2.

2.3 Fiber Interferometer

The fiber interferometer is essential for the detection of small motions. A basic outline of the interferometer system is shown in Figure 2.6.

Light emitted from the laser diode is coupled to the fiber, then sent to a directional coupler and split down in two directions. We use only one of the arms of the fiber for detection, the lower one of the right side of Figure 2.6. Light partially internally reflects from a nicely cleaved end of the fiber ($\leq 4\%$) and partially transmits out. Transmitted power reflects back from the oscillator and re-enters the fiber thus forming an interference with the reflected light from the cleaved end that is detected at the photodiode. Neglecting multiple reflections, one can

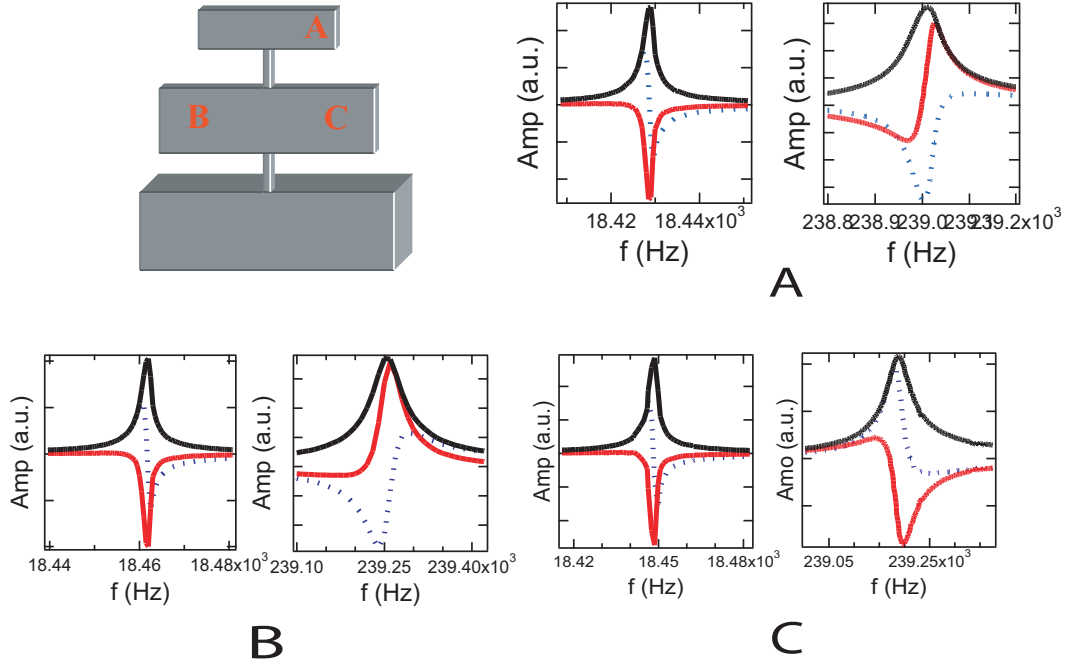


Figure 2.5: Phase sensitive detection showing lower cantilever and upper (antisymmetric) torsional mode with the measurements done at three points of the cantilever. X (blue dashed line), Y (red solid line) indicate that oscillation at point A, B and C are in phase for lower cantilever. X and Y are in phase for points A and C and out of phase with B for upper torsional mode.

easily write down the net intensity of interfering light of wavelength λ for a fiber to oscillator separation of x :

$$I = I_0[R_{cleave} + (1 - R_{osc})^2 R_{osc} + 2(1 - R_{cleave})\sqrt{R_{osc}R_{cleave}} \cos(\frac{4\pi x}{\lambda})] \quad (2.3)$$

where R_{osc} and R_{cleave} are the reflectance of the oscillator and the cleaved end of the fiber, respectively.

Our interferometer system consists of a 1 mW infrared laser diode, with a wavelength of 1310 nm ordered from PD-LD Inc. The laser is then coupled to the input of a Gould 10-0003 Singlemode 9/125 fiber. A photodiode, also supplied by

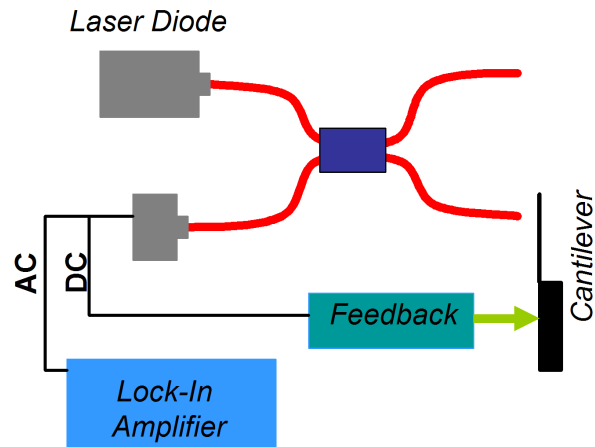


Figure 2.6: Outline of the interferometer system.

PD-LD, is coupled to the other input and is used to measure the intensity of the light reflected from the cantilever end of the fiber. The photodiode consists of a very simple $I - V$ converter as shown in Figure 2.7.

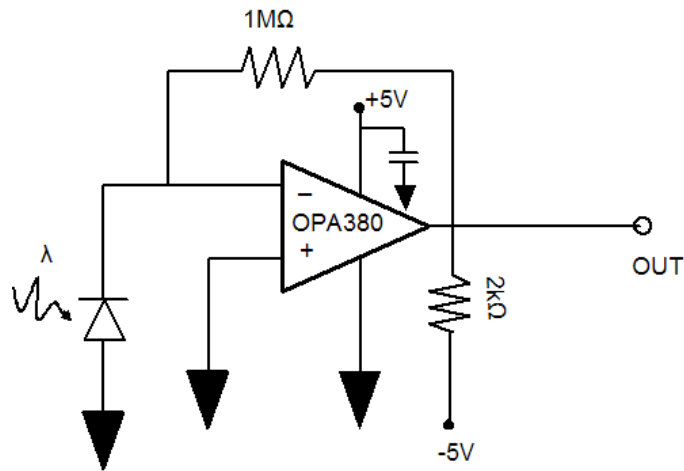


Figure 2.7: Photodiode circuit for Fiber Interferometer.

The responsivity of the photodiode is 0.8 A/W and usually only $\sim 10\%$ of the laser power can be successfully coupled to the fiber. Assuming that we will get $\sim 4\%$ of that light at the photodiode, we can estimate the Voltage output of the

converter to be $V = (0.1 \times 0.04 \times 1 \text{ mW}) \times 0.8 \text{ A/W} \times 10^6 \Omega = 3.2 \text{ V}$.

Prior to the infrared laser I had been using a 10 mW red laser with a wavelength of 678 nm. The use of this laser lead to cantilever heating¹. That same 10 mW red laser diode had a built-in regulator circuit that would only allow it to operate in constant power mode². This would result in instability of the output power due to some of the reflected light entering back into the laser diode. The infrared laser that we started using later is operated in constant current mode and is more stable.

2.4 Feedback

In order to make sensible motion measurements of the cantilever we want the voltage output of the photodiode circuit to scale linearly with the displacement. This can be easily achieved by fixing the fiber to oscillator distance to be odd multiples of $\lambda/4$, a quarter wavelength of the laser. The reason for this is that the separation between the two intensity peaks is $\lambda/2$, and the sine or cosine is very linear where the slope of the tangent line is the steepest. If the oscillator is experiencing very small oscillations in this region one can approximately convert the measured AC voltage to the distance by multiplying the inverse slope of interference intensity (Figure 2.8), $V = \frac{V_{max}+V_{min}}{2} + \frac{V_{max}-V_{min}}{2} \cos(\frac{4\pi}{\lambda}x + \varphi_0)$ to the measured AC signal:

$$x_{AC} = \frac{V_{AC}}{V_{max} - V_{min}} \times \frac{\lambda/4}{\pi/2} \quad (2.4)$$

In order to be able to lock the spacing between the cantilever and fiber to the steepest part of the slope where the relation between the voltage and distance is

¹The optical absorption for silicon increases sharply for photon energies above the band gap energy of 1.12 eV.

²The red laser diode had a built-in photodiode to keep track of the and feedback to the laser.

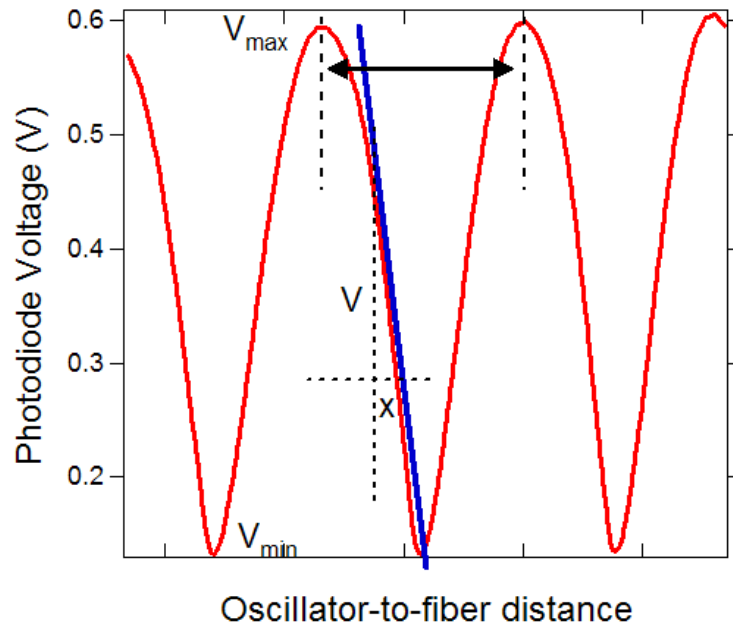


Figure 2.8: Interference pattern measured by a photodiode, usually referred as the DC level. Distance between two peaks is a half wavelength of a 678 nm laser diode.

linear, we use the feedback circuit shown in Figure 2.9. The difference amplifier can set the desired voltage $(V_{max} - V_{min})/2$ on the fringe. When the integrator is turned on, the difference amplifier spits out the voltage difference between the output of the piezo and the set value³.

The gain of the proportional amplifier and the integrator can be adjusted through the variable resistors depending on the size of the fringe. The fringe slope inverter gives flexibility for locking the voltage of the fringe either to the negative or positive slope.

³Output of the piezo is wired to the one of inputs (DC Ref.) of the difference amplifier even though the wiring is not shown in Figure 2.9.

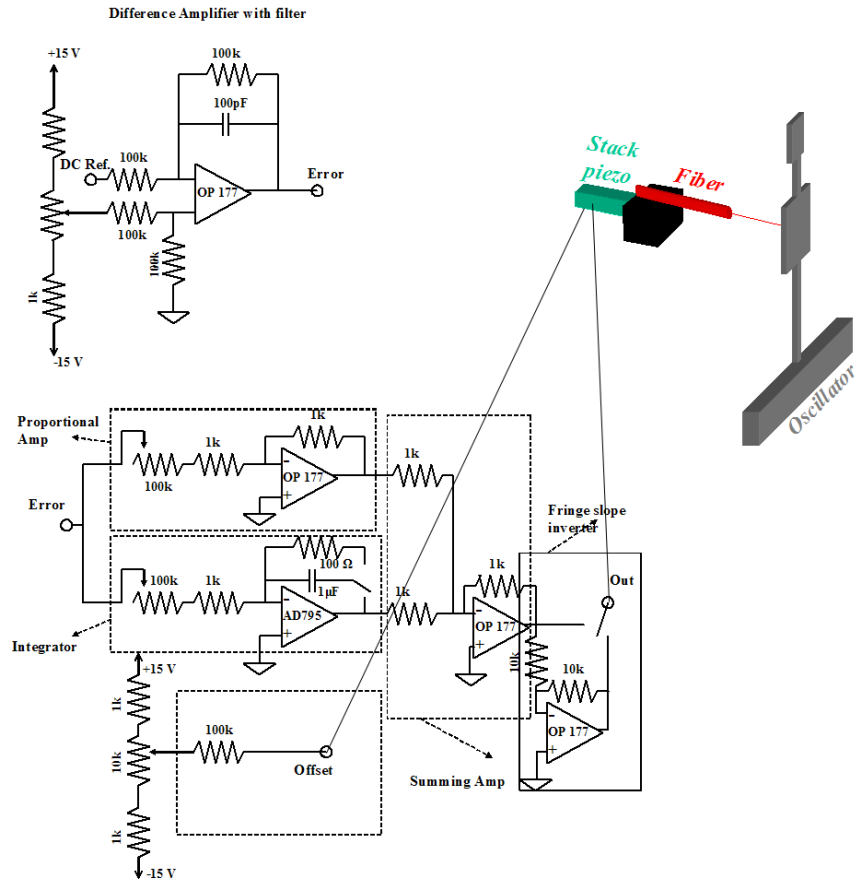


Figure 2.9: Feedback circuit to maintain oscillator to fiber end distance constant.

2.5 Careful Lock-In Detection

Lock in detection is widely used in different areas of solid state physics, especially transport measurements, where one tries to get away from the $1/f$ noise, white noise and other unwanted periodic oscillations (*i.g.* line interference). In our particular experimental setup we used lock-in detection to measure the oscillation of the cantilever at its resonance frequency by setting the reference frequency of the lock-in to the same value. Since we used the lock in to measure very small signals and sometimes we need to deal with a signal buried in thermal noise we need to

isolate all the possible sources of noise. The resonant frequency of the cantilever is in the kHz range so we can safely install high pass filters before the inputs of the lock-in amplifier. It is also very important to connect all the detection equipment and the electronics that go inside the probe to the same power outlet. This will help to remove ground loops. Mechanical Isolation of the probe or other equivalent techniques will also improve the performance of the detection.

When all the necessary precautions are taken we are ready to make our measurements. Choosing lock-in settings very much depends on the measurement we are performing. The relation between the bandwidth and the time constant of the SR830 lock-in is given by $\Delta f = 1/(4\tau)$. Smaller bandwidth means smaller noise but it also means a longer time⁴ is needed to detect the fully recovered signal (Figure 2.10). This will cause problems if the signal doesn't stay constant for a long time (i.e., modulated nuclear magnetization will decay and will not be there forever.) This problem can be overcome by simply increasing the bandwidth and averaging to get a better Signal to Noise Ratio (SNR).

2.6 Multi-functional Piezo Scanner and Coarse Approach

We have used model EBL-2 Tube piezo from Staveley NDT Technologies to make our built in scanner and coarse approach mechanism. The dimensions of the piezo tube are 1 inch in length and 0.335 and 0.375 inches in inner and outer diameter, respectively. The piezo is attached to a macor mount and then to the main aluminium body supporting the stage. The stage proved to be reasonably reliable for positioning a 2 mm diameter iron magnetic sphere inside the magnetic field.

The coarse motion was achieved by feeding high quality sawtooth voltage signals to the four quadrants of the piezo. The inner electrode was grounded at all

⁴The lock-in manual suggests that the wait time should be around 5τ to detect the maximum signal when the filter slope is set to 6 dB/octave.

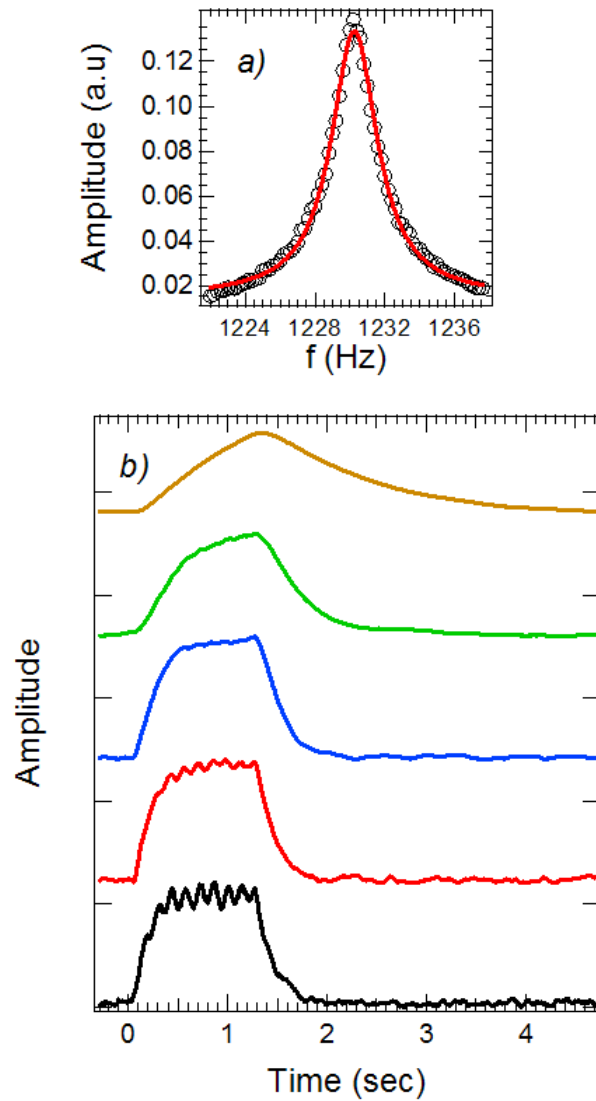


Figure 2.10: a) The driven scan of the cantilever with $f_0 = 1230$ Hz and $Q = 830$ fitted with a Lorentzian curve. b) The lock-in measurement of the driven scan with time constants of 10 ms, 30 ms, 100 ms, 300 ms, 1 s from bottom to top respectively.

times. The sawtooth is generated by a *LabView* program and fed into a *DAQ* card. Analog output voltage is then amplified and applied to the tube piezo. 2.11.

The sawtooth voltage applied to the piezo extends the piezo during the slow

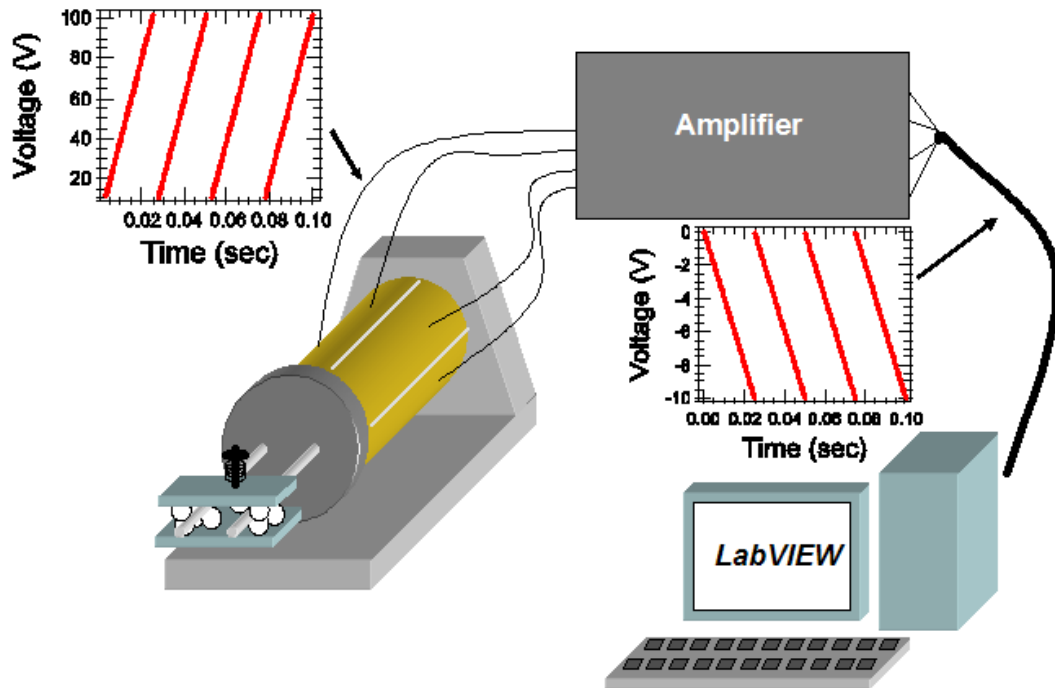


Figure 2.11: Coarse z approach system with xyz scanning capabilities.

ramp. The translation stage moves with the piezo because of the static friction force between the sapphire balls and sapphire rails. During the fast ramp the inertia of the stage is large enough to overcome the static friction, and the stage slips, that is, it remains stationary while the piezo moves. Applying a periodic slow ramp-fast ramp causes a similar stick-slip motion in most inertial drive designs [15], [16], [17]. When the magnetic sphere finishes approaching the cantilever and is at the desired position, I usually switch all four quadrants of the piezo to ground.

The translation stage is made of SS-304 attached sapphire balls. The arrangement of sapphire balls forms a smooth groove, thus allowing the stage to slide on cylindrical sapphire rails as shown in Figure 2.11.

The amplifier we have assembled for the tube piezo consists of a very simple homebuilt DC power source and four PA 142 power amplifiers from APEX Tech-

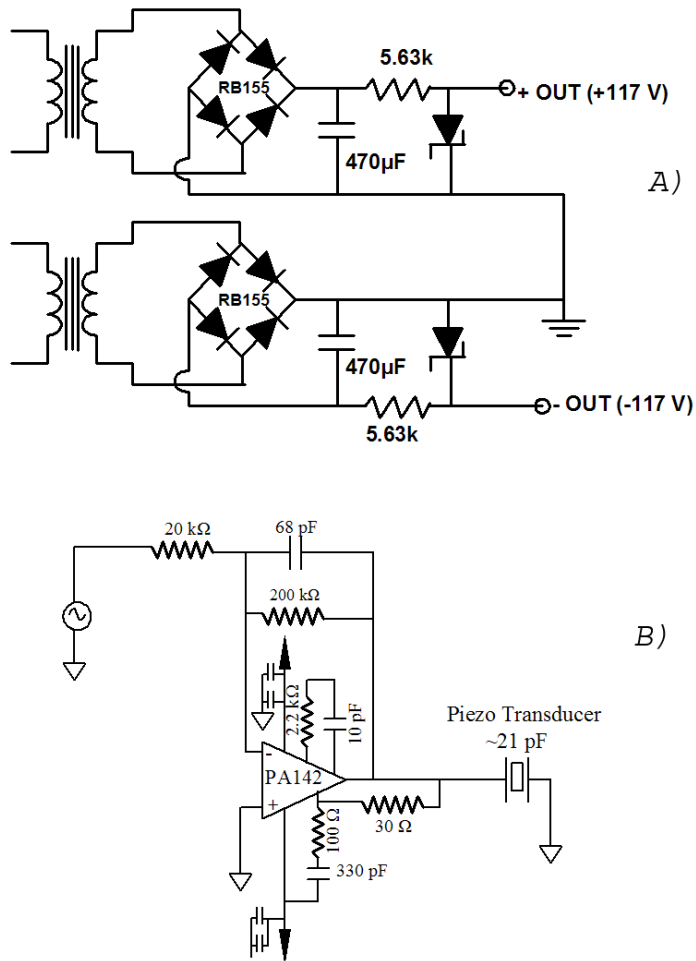


Figure 2.12: a) DC supply and b) amplifier for Tube Piezo.

nologies.

The xyz scanning can be achieved by applying the voltage to corresponding quadrants. For example applying negative (positive) voltage to all four quadrants will extend (shrink) the piezo, moving the stage forward. Applying negative (positive) voltage to the right quadrant and positive (negative) to the left quadrant will move the stage to the right (left). We never needed to use the lateral scanning

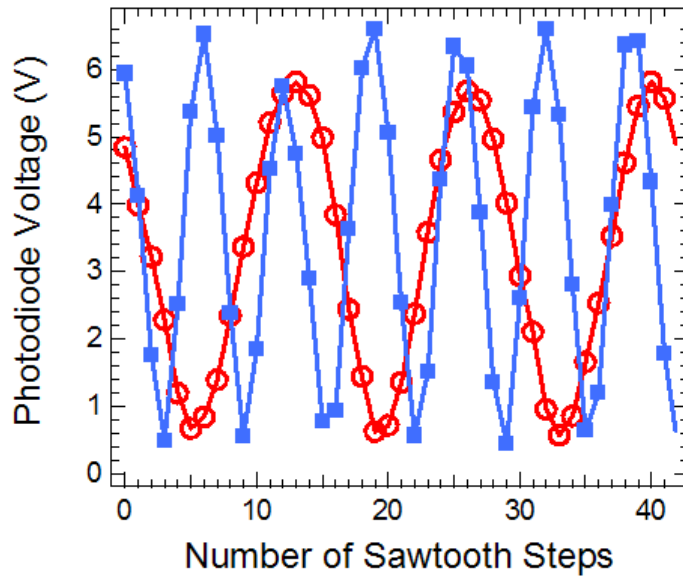


Figure 2.13: Photodiode voltage versus number of sawtooth steps applied to move the stage with roughly ~ 1 gram of additional weight down (solid squares) and up (open circles) clearly reveals the reliable motion of the stage in z direction.

mode in our experiment but it will be useful for the magnet on oscillator geometry to precisely position the sample.

2.7 Permanent Magnet

I have used an iron sphere as the permanent magnet to produce the field gradient necessary for an NMRFM experiment. It was prepared from 99.99% purity iron by arc melting and letting the surface tension form the sphere. It usually takes 3-4 tries to get a shape that is close to a sphere shape. There are two reasons why iron was chosen over commercially available Nd-Fe-B or other alloy magnets. First, iron has a larger magnetization than cobalt, nickel or many other magnetic alloys. Second, iron is a very soft magnet, meaning the magnetization will always point along the applied field and there will be no magnetic torque due to the external field that might

rip the magnet out of the stage. The field produced by the uniformly magnetized

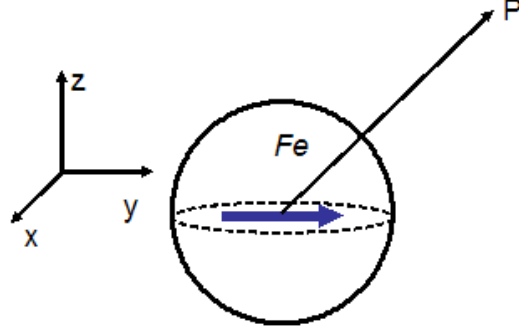


Figure 2.14: Magnetized iron sphere.

sphere of radius a and magnetization \mathbf{M} at point P outside the sphere is equivalent to the the field produced by a magnetic dipole with a moment of $\mathbf{m} = 4\pi a^3 \mathbf{M}/3$. So the field for a uniformly magnetized sphere shown in Figure 2.14 is:

$$\mathbf{B}(\mathbf{r}) = \frac{\mu_0 M a^3}{3r^3} \left(\frac{3xy}{r^2} \hat{\mathbf{x}} + \frac{3y^2 - r^2}{r^2} \hat{\mathbf{y}} + \frac{3yz}{r^2} \hat{\mathbf{z}} \right) \quad (2.5)$$

The net equilibrium nuclear magnetization of the sample will line up with the external field in the y direction for the geometry of the current experiment. Also, since the motion of the cantilever is in the $y - z$ plane, we need to consider only the force induced on the cantilever in the z direction due to the coupling of the moment in the y direction to the field gradient B_y

$$\begin{aligned} F_z &= \nabla_z(\mu \mathbf{B}) = \mu \frac{\partial B_y}{\partial z} \\ \frac{\partial B_y}{\partial z} &= \frac{\mu_0 M a^3 z}{r^5} \left(1 - \left(\frac{y}{r} \right)^2 \right) \end{aligned} \quad (2.6)$$

Based on our calculations of the field and field gradient we can optimize the signal by carefully adjusting the sample-magnet separation.

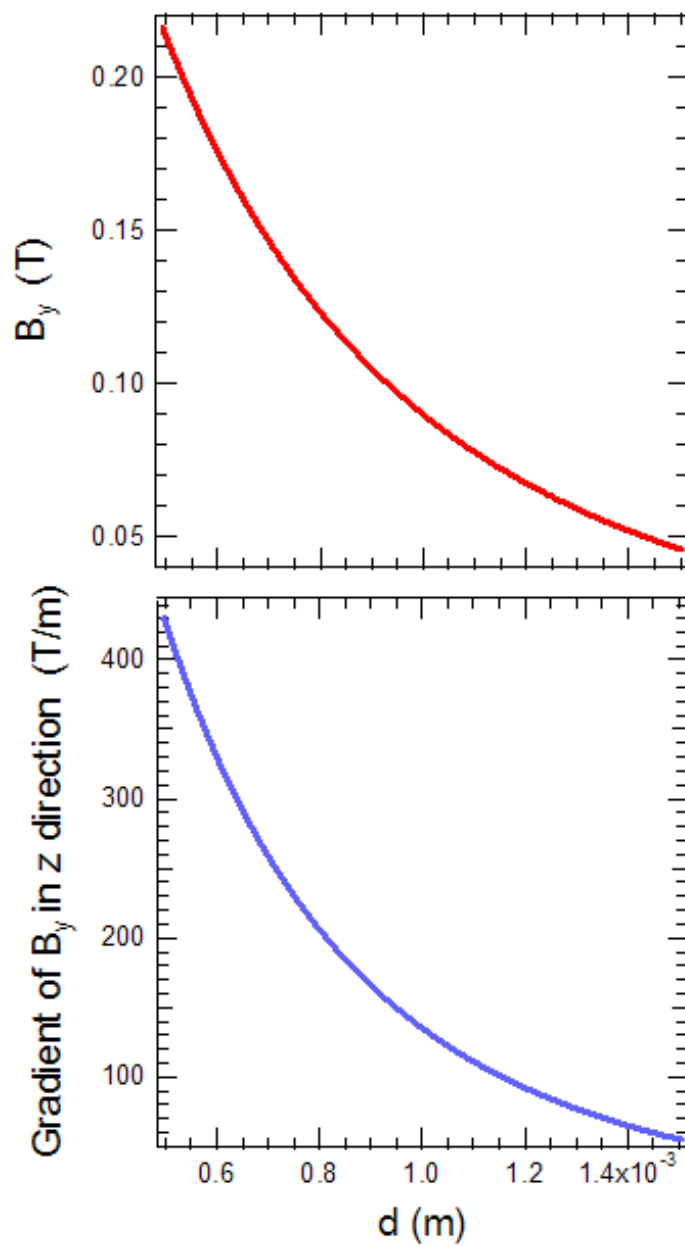


Figure 2.15: Component of the field along $-y$ direction (top) and its gradient in the z direction (bottom) versus the distance from the surface of the magnet in the z direction $(0, 0, d)$ induced by an iron sphere 2 mm in diameter.

2.8 RF Coil and Tuning Capacitors

The needed RF field for spin resonance was provided with a coil made out of 32 AWG with *Niclad* coating on it. The coil has 9.5 turns, a length of 2 mm and diameter of 1.5 mm. After the coil was wound, I coated the outside of the coil with Torr Seal epoxy so that it would retain its shape.

In order to efficiently transmit the RF power from the source, in our case an RF amplifier, into the coil we had to maintain matching impedances throughout the entire path from the amplifier to the coil. Most commercially available RF units have input and output impedances of 50 Ω . The RF signal generator, RF pulse programmer and RF amplifier are all connected with either RGA-174 or RG-58 50 Ω transmission lines. So the only thing we should really be careful about is the RF coil. The 50 Ω matching is achieved by adding RF capacitors and forming an *LRC* circuit.

There is a lot of literature about RF design and some very informative references specifically about tuning NMR coils [18]. Detailed circuit analysis is not a very efficient way of tackling the tuning process. Instead, one should follow the recipe below for fast tuning. Once the coil is ready and its inductance is measured⁵, is measured one can roughly estimate the desired in-series capacitor needed by $\omega L = (\omega C)^{-1}$. The value of the parallel capacitor can be found by directly connecting different value capacitors to the circuit and trying to tune it until it works⁶. If tuning can't be achieved this way, it also worth trying to reverse the order of capacitors (i.e. connect in series capacitors to the parallel combination of coil and capacitor). Our tuning was performed with a HP8753B Network Analyzer which

⁵It is important for the coil to have inductive impedance (i.e. to be in the upper half of a Smith chart), since only capacitors will be added to achieve the desired tuning. Sometimes it just happens that the impedance of the coil is capacitive but this can be overcome by simply changing the number of turns in the coil or adding extra length to the cable between in-series capacitor and coil.

⁶This seemingly sloppy technique worked out well for me for tuning three different coils

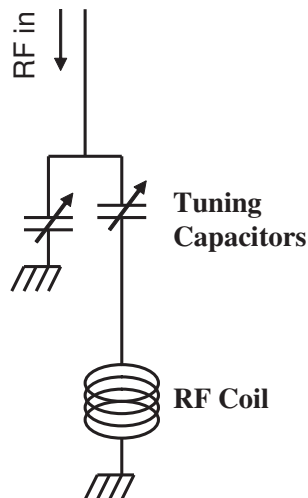


Figure 2.16: Outline of the RF coil and tuning circuit.

measures impedance directly

Other technical details that must be properly executed for good RF coil circuitry are: Making the non-coaxial wires used in the circuit rigid for reliable tuning and removing sharp points by covering them in solder to prevent unwanted arcing.

Putting the tuning capacitors close to the coil minimizes the amount of resistive wire in LRC circuit, and thus will enhance the quality factor of the tuning circuit which is important for conventional NMR to increase pick up of the induced voltage. However for NMRFM, where the induced signal is detected by a mechanical resonator, it also helps by sending less RF power into the coil to prevent various spurious excitations of the cantilever.

2.9 RF Modulation Electronics

As was carefully explained in Section 1.2, in order to detect the nuclear spin through NMRFM we need to decay slowly to the Larmor frequency and start the frequency

modulation of RF power at the cantilever's resonance frequency. Most commercially available RF signal generators have options to modulate phase, amplitude, and most importantly frequency with the external input either through AC or DC coupling of the modulation voltage. We use the DC coupling option to modulate the frequency.

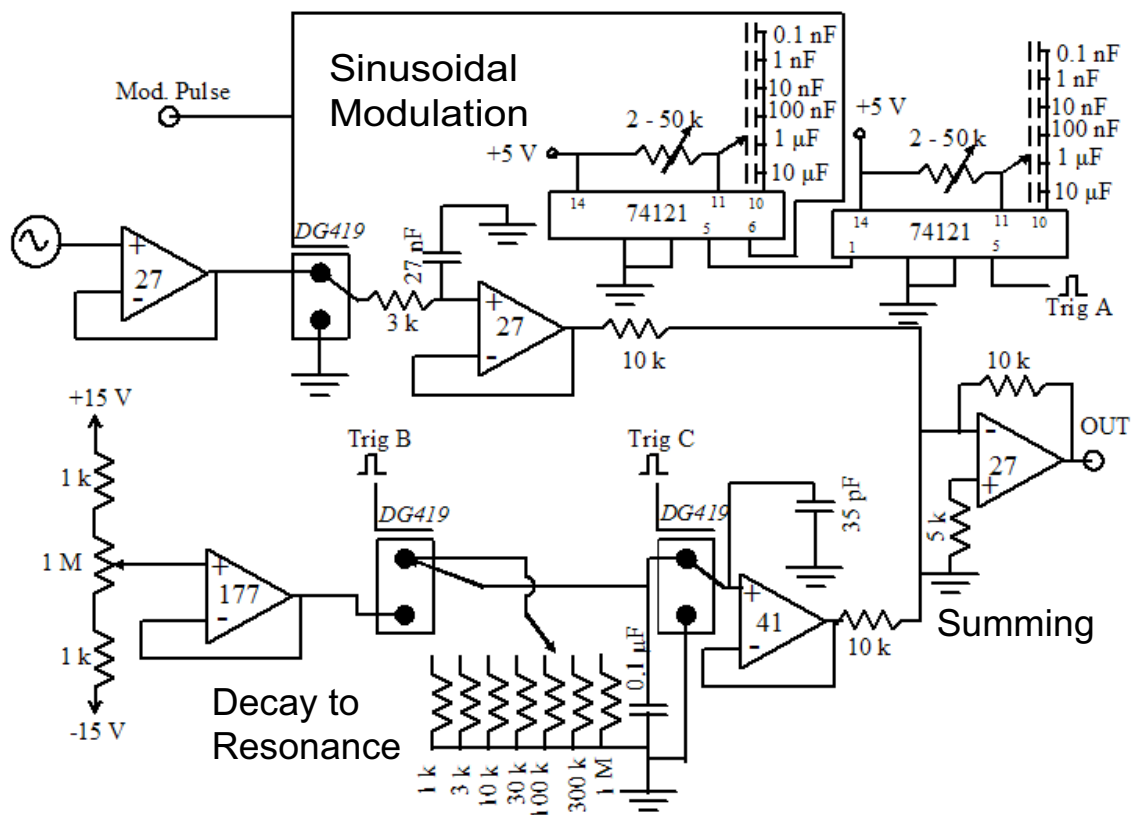


Figure 2.17: Outline of the RF modulation electronics. All the switches in the diagram are shown in the triggered position.

The operation of the modulation electronics shown in the Figure 2.17 is very simple. The sine wave that determines the modulation frequency is constantly

fed into the box. The switch DG419 controlled by the combination of two 74121 monostable multivibrators determine when to let the modulation sine wave in or ground the input. When the first 74121 is triggered by the positive slope of input pulse A it determines the time before triggering the second multivibrator. When the second multivibrator is triggered it sets how long it should keep the switch on (let the modulation wave in). When the time set by an external RC circuit element expires, the switch will connect to the ground thus stopping modulation input into the box. The RC circuit connected before the voltage follower ensures that there are no sudden jumps when the switch connects the input to the AC signal generator.

The second part of the electronics is responsible for the smooth decay of the carrier frequency from off resonance to resonance at the Larmor frequency. Since the modulation input of our Rhode & Schwartz RF signal generator only takes 1 V_{pp} input, only a small part of the the 30 V offset range is used. But nevertheless we have it. The variable resistor sets the peak value from which the voltage starts decaying to 0 V. Before the pulse B triggers the switch, it is connected to the offset voltage and the capacitor will be fully charged. But once the switch is triggered, it connects the capacitor to the selected resistor, and this causes an exponential decay with time constant $\tau = RC$. The next switch lets the decaying voltage pass through when triggered by pulse C . A 35 pF capacitor connected right after the switch is used to remove the transient effects of the switch.

The voltage output of the decay and sine modulation gets added at the summing amplifier and sent to the output. The purpose of connecting the voltage followers before the inputs of the summing amplifier is to remove the cross talk between the decay and modulation signals. It prevents the voltage of one of them from affecting the voltage of the other.

This box is very versatile and we use it in combination with an already existing simple pulse programmer.

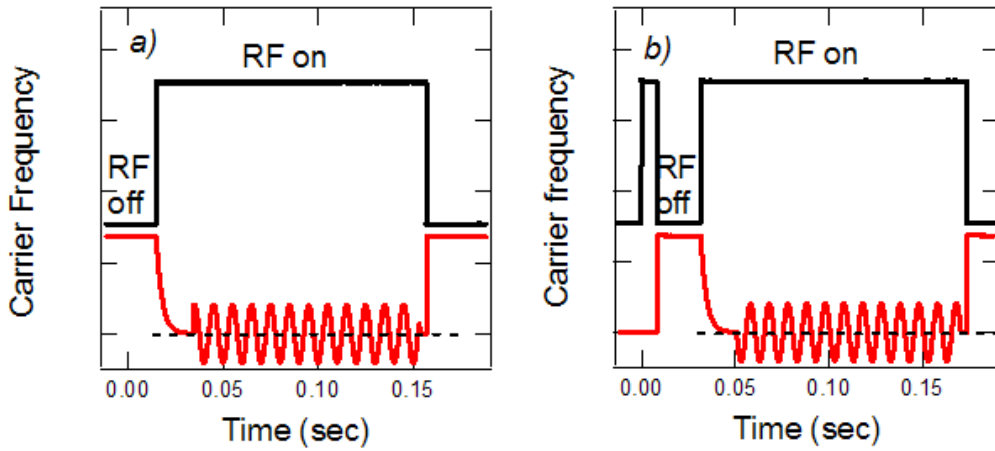


Figure 2.18: Output of the pulse programmer (black curves) and modulation box (red curves). RF off corresponds to zero power output. a) Modulation sequence widely used in imaging. b) Sequence used for spin nutation and for T_1 measurement.

Figure 2.18 gives some examples of the modulation electronics and pulse programmer in operation. In Figure 2.18a one single pulse triggers all pulse inputs at the same time. This kind of the modulation sequence is used for imaging purposes, RF power gets turned on at the off-resonance frequency and smoothly decays to the Larmor resonance value. When the decay is complete the frequency is modulated at the cantilever's resonance frequency.

If we recall from Section 1.1 the pulse width required to tilt the net nuclear spin by an angle θ is $t_\theta = \theta/(\gamma B_1)$. A spin nutation experiment is one where the nuclear spins are tilted by an RF pulse and then sampled so one can observe the oscillating behavior of the magnetization as a function of tip angle. In order to observe the spin nutation the time between the rotation pulse and the sampling (modulation scheme) must be $T_2^* \ll \tau \ll T_1$. In our experiment T_2^* has no physical importance and in our setup it is dominated by the inhomogeneity of the field due to the presence of the permanent magnet. In conventional NMR experiments it is

mainly due to the inhomogeneity of the external field⁷.

Figure 2.18b shows a different pulse and modulation sequence that can be used for the nutation and T_1 measurement. A nutation measurement can be done by changing the width of the on-resonance pulse and the T_1 measurement can be done by setting the pulse width to a π pulse, the pulse required to tilt the magnetization by an angle π , and performing this measurement for different values of the waiting time between the π pulse and the sampling (modulation) sequence allows one to measure the recovery time for the z component of the magnetization.

2.10 Technical Challenges

The major problems that I will address here are related mostly to the sample and cantilever. Our first attempt was to study metal hydride films directly deposited on the cantilever by e-beam evaporation. Even though this attempt was abandoned after 5 month of effort, it is worth mentioning some things about the problems encountered. Cantilevers were masked to allow the deposition on the selected region of the oscillator. First, a 500 to 1000 nm yttrium (Y) layer was deposited and then capped with 30-50 nm layer of palladium (Pd). The very first time I did this, I realized that the lattice expansion of yttrium during the hydrogen loading bends the cantilever, making it useless. In subsequent attempts I flushed the chamber with hydrogen so that there was a hydrogen background during the evaporation. This hydrogen would be absorbed during the evaporation and form YH_{2-x} reducing the stretch of the cantilever later when an additional amount of the hydrogen gas was forced into the film. Another problem is that the mask would shift and film would get deposited on the neck of the cantilever thus drastically reducing its quality factor (Figure 2.19).

⁷ $1/T_2^* = 1/(2T_1) + 1/T_2 + \gamma\Delta H$, In the case of our NMRFM experiment the field gradient is on the order of 10^2 T/m and the sample thickness of $20 \mu m$ will result in $1/T_2^* \simeq \gamma\Delta H \sim 10\mu s$.

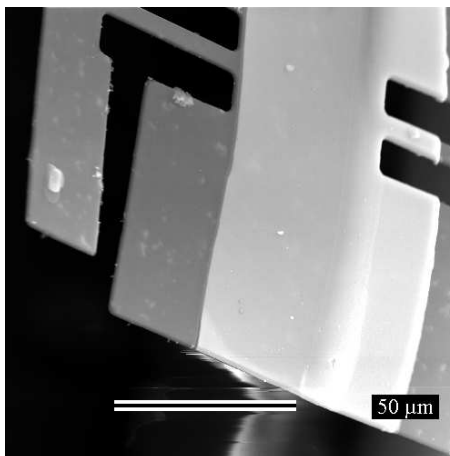


Figure 2.19: SEM image of the double torsional oscillator coated with Y and Pd metals. The image shows how a masking problem resulted in the film coating the lower neck of the oscillator.

The reason we abandoned the yttrium hydride study was because we failed to see any NMR signal from it. We suspect that once I started pumping the probe the yttrium hydride was giving away some of the hydrogen and becoming YH_{2-x} . This sample would have short T_1 and $T_{1\rho}$ making the NMR signal decay too short to measure with cyclic inversion.

Our next sample of the choice was ammonium dihydrogen phosphate ($(NH_4)H_2PO_3$), or ADP. This sample was commercially available and was stable under normal conditions making it easy to attach to the oscillator. I tried to attach the sample to the oscillator by vacuum grease, as has been done with other previous samples [20]. However, every time I did that, and put the oscillator into the probe, I would lose the sample. It would simply get loose and shaken off. Since this happened before I applied the RF power, laser heating became the first suspect. The softened grease would not provide enough stiction to hold the sample. Next, the sample was glued to the oscillator by silver epoxy. The sample stayed fixed but at high enough vacuum inside the probe (lower than 10^{-4} torr), the sample melted as shown in Figure 2.20. The 678 nm wavelength of the laser happens to be right at the band gap energy of

the silicon and readily absorbed by the cantilever. Even though this absorption of

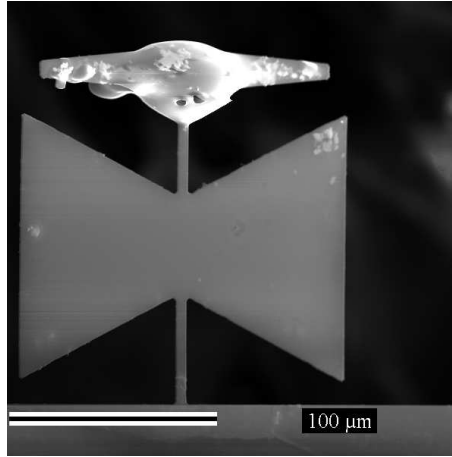


Figure 2.20: SEM image of the melted ammonium dihydrogen phosphate (ADP) covering the entire head of the double torsional oscillator.

laser power proved to be fatal for our sample, it might be extremely useful for carrying out higher temperature NMRFM experiments. Most of the NMRFM probes have delicate parts that cannot tolerate much heating, and this technique of locally heating the microsamples might be a good way around it.

In order to avoid melting of the sample we have replaced our interferometer with the infrared interferometer system discussed in Section 2.3. Changing the interferometer solved this problem.

Figure 2.21 shows a successful attempt of gluing the sample to the oscillator. In good vacuum a long exposure to the high RF field will also melt the sample, so I kept the cyclic adiabatic inversion time below 500 ms, with a repetition period of 10 s.

Another problem associated with the RF heating is the shift of the resonance frequency of the cantilever. The shift in resonant frequency reduces the measured amplitude of the signal, but even worse the change in frequency during the modulation time would yield an unreliable relation between the amplitude and the real

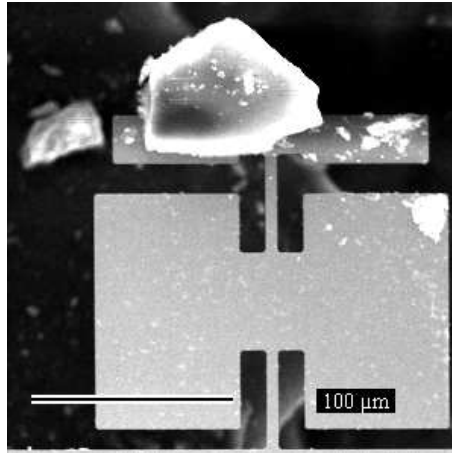


Figure 2.21: SEM image of the ADP glued to the double torsional oscillator.

magnetization under the investigation. Figure 2.22 shows a quasi-static shift of resonance frequency of the oscillator. RF power was sent to the coil for 500 ms with the repetition period of 10 s and the frequency was measured after 15-20 cycles.

The way around this problem for me was to reduce the quality factor, Q , of the cantilever by putting an extremely small drop of silver epoxy at the lower neck of the cantilever close to the base. This reduced the Q from 2000 down to roughly 500. Now the small changes in frequency would not result in a strong change of measured signal. Of course this is not the ideal way of solving this problem; the better way might be to minimize the heating by implementing a different kind of sampling technique that would not require continuous blasts of the RF field.

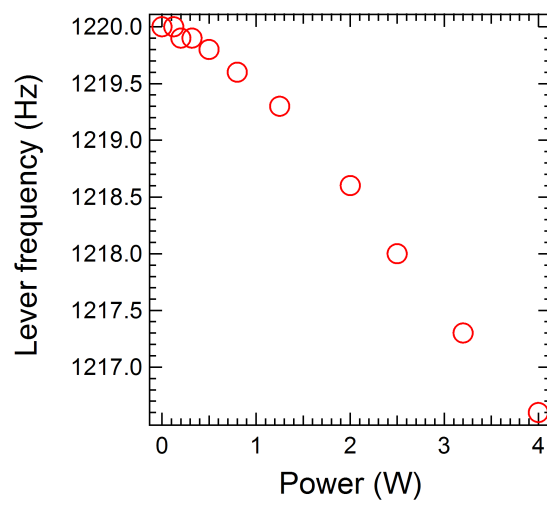


Figure 2.22: Change in the resonance frequency of the cantilever due to the RF power sent to the coil. The frequency modulated RF power pulses were sent to the coil for 500 ms with 10 seconds repetition time.

Chapter 3

Cavity Induced Self-Sustained Oscillations of Micro Cantilevers

In these next two chapters we will take a slight detour from my main experiment and will explore two important phenomena, self oscillation of cantilevers and coupling of magnetically coated cantilevers to the external magnetic field. Systematic characterization of these phenomena are very important since the cantilever is used for detection of small forces.

3.1 Brief Overview of Self Oscillations

As seen from the earlier discussion in Section 2.3 fiber optic interferometers, due to their high sensitivity, are an integral part of most techniques that use mechanical detection of sensitive micro resonators [23], [24]. These highly sensitive micro resonators are capable of large responses to very small forces at their resonant frequencies. Ideally the effects of the laser radiation used for motion detection are negligible, however coupling between the laser radiation and mechanical oscillator is possible in more realistic systems. This coupling might result in a wide range

of effects including self sustained oscillations which we will discuss here. Self sustained oscillation is the phenomenon where a cantilever, under the influence of only laser power and no deliberate driving force, can start oscillating at its resonant frequency. This effect was first observed in metal coated micro-mechanical cantilevers [25]. Most of the reports of self-sustained oscillations have been done for cantilevers coated with a thin metallic layer. Further studies of these bi-metal cantilevers shed more light on how this phenomenon works, and actually some have utilized this phenomenon to drive [26] and laser cooling of the cantilevers [27]. The same has been shown for silicon resonators with a sufficiently thick oxide layer, where a matching of the heat diffusion time constant to the resonance frequency of the microstructure gives rise to a driving force.

At first glance the phenomena of self oscillation seems to be very odd: How can a DC laser power input drive a cantilever to oscillate? Before answering this question it would be useful to consider a more obvious case. Let's modulate the laser power shining on the bi-metal cantilever at the cantilever's resonant frequency. It is not beyond the realm of possibility to expect oscillations, and indeed they have been observed [28]. The authors of Ref. [28] claim that the origin of the oscillation is the modulated thermal stress generated by the laser power. Two different materials experience different thermal expansion resulting in a bending of the cantilever. However, the authors fail to effectively rule out the contribution of modulated radiation pressure that might also result in excitation of the cantilever. Another work that utilized modulated laser power to drive the cantilevers delivers a more insightful understanding and successfully demonstrates that, indeed, modulated thermal stress is the origin of the driving force [29]. In their setup they apply modulated laser power at the base of the cantilever rather than directly on the body of the structure. This to some degree will eliminate the excitation due to radiation pressure. And the authors very confidently infer that modulated heat diffusing into the

structure from the base is driving the cantilever. It is thus not very surprising to observe oscillations when the laser power is modulated at the oscillator's resonant frequency, be it due to the modulated heat diffusion or radiation pressure force.

The effect of the DC laser power is a little bit trickier. To the best of our knowledge, all the reports of self induced oscillations have been observed only on bi-metal cantilevers, except a single case where it has been seen in a cantilever with no coating [19]. The key point for the self-sustained oscillation is the formation of an optical cavity. As described in Section 2.1, in order to measure the displacement of the cantilever we lock the fiber-to-cantilever separation to the linear part of the interference fringe (Fig. 3.2 a), thus forming an optical cavity. We can either lock the position so that the slope of the linear region is positive (red detuning) or negative (blue detuning). If the cavity detuning is locked to red, then the cantilever will bend and move back where the intensity of the light is less. This in turn will result in cooling of the cantilever restoring it to its original position. This oscillation happens at the cantilever's resonance frequency. Thus, the thermal stress due to the different thermal stress caused by different expansion of the silicon and coating material will drive the cantilever. When the cavity detuning is blue then this same effect will act as a negative feedback (i.e. heating will push the lever to the region with higher intensity and thermal stress will oppose the restoring force) thus suppressing the motion.

One important thing to note is that the thermal stress is a nonlinear force. The reason is that there is a delay between the instant when the photons strike the lever and the thermal response of the cantilever due to the heat diffusion time constant. This phase lag between the thermal response and motion of the cantilever is an essential mechanism for driving. If the force was linear (i.e. radiation pressure) and had the same phase as the displacement of the cantilever, then this force would only affect the effective spring constant of the cantilever. With this in

mind we should move on to our experiment where we have used single crystal silicon cantilevers with no metal or oxide coating.

3.2 Self oscillation of a Single Crystal Silicon Cantilever

Our experimental setup and an SEM image of the single crystal silicon cantilever we have used are shown in Figure 3.1 (a), (b). A 10 mW laser with wavelength 678 nm was used both for applying radiation power and for displacement detection. The maximum power at the cantilever end of the fiber was measured to be around 1 mW. The experiment was carried out at a base pressure of 5×10^{-4} torr to reduce air damping. A feedback loop with a high frequency cutoff of 250 Hz was used to compensate for unwanted mechanical drifts between the fiber and the cantilever while measuring Brownian noise and driven spectra. The fundamental flexural mode resonance frequency for the cantilevers is 3.7 and 6.4 kHz for thicknesses of 390 and 570 nm, respectively.

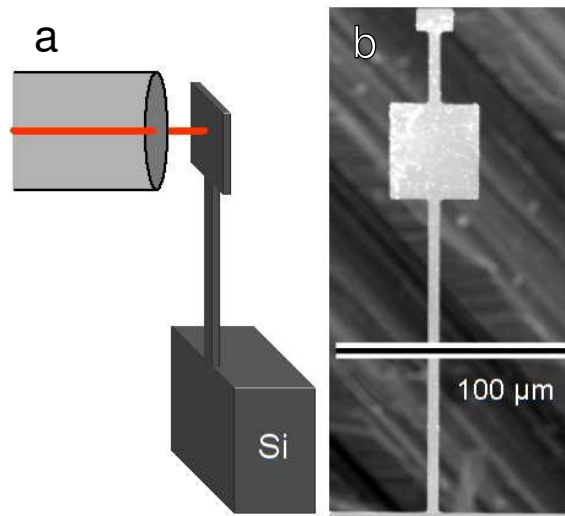


Figure 3.1: a) Image of the experimental setup and b) an SEM image of the paddle cantilever used in this study.

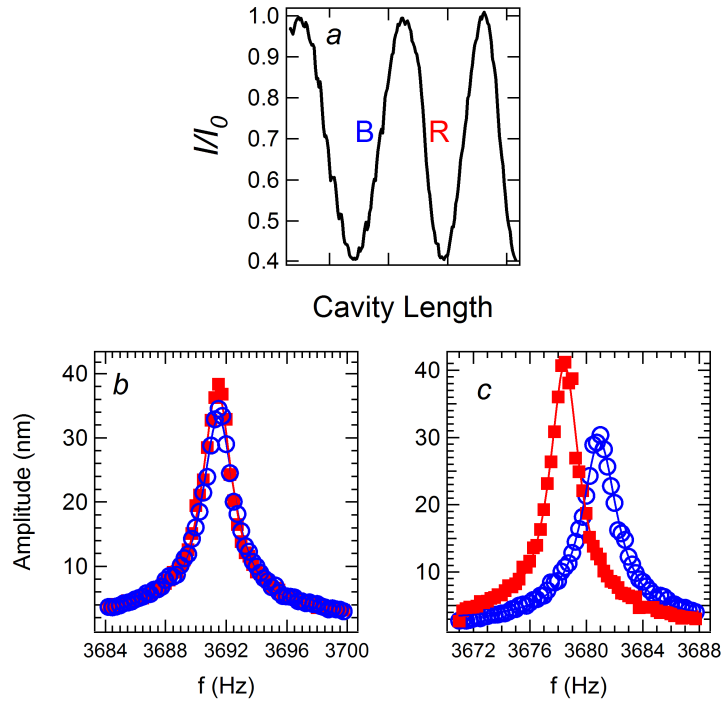


Figure 3.2: a) Normalized intensity versus cantilever-fiber distance measured with the photodiode. Letters B and R stand for blue and red detuning respectively. The driven scans obtained at b) 40 and c) 750 μW .

One of the empirical observations is that on different sides of detuning¹ the measured driven scans differ from each other at higher laser power. Scans on the red side of the fringe result in a bigger driven amplitude and lower resonance frequency compared to the scans obtained on the blue side of the interference fringe, see Figure 3.2.

The observed frequency difference between the two sides of detuning can be explained by writing down the equation of the motion.

¹The resonance in an optical cavity occurs when the cavity length is an integer multiple of $\lambda/2$. The left and right sides of the resonance are referred as blue and red detuning, respectively

$$\begin{aligned}
m\ddot{x} - \gamma\dot{x} + kx &= F_{rad} \\
F_{rad} &= F_0 + \frac{\epsilon P}{c} = -\frac{\alpha\epsilon x}{c}
\end{aligned}
\tag{3.1}$$

where F_{rad} is the pressure exerted by the laser beam. ϵ , α and c are the fraction of the momentum transfer, slope of the power gradient, $\Delta P/\Delta x$, and the speed of light, respectively. The sign of the slope α determines whether the frequency is shifted right or left.

The observation of different amplitudes for the same driving force suggests that laser radiation in a cavity couples to the mechanical motion of the single crystal silicon cantilever². At present we do not have a coherent analytical model of the system. In order to better characterize this behavior we did some careful studies of Brownian noise measurements taken with a Fast Fourier Transform (FFT) Analyzer. These measurements showed that Brownian noise is in fact enhanced for the red side of the cavity compared to the blue (Figure 3.3). Also the decrease of the resonance frequency, regardless of the side of the fringe, is observed and we attribute it to static heating of the cantilever³. Laser radiation absorbed by the cantilever will raise the temperature of the microstructure; poor conduction of heat through the long neck and poor dissipation of heat in a vacuum are the key reasons for this. Enhancement of the Brownian noise must be considered very seriously since these soft cantilevers are used to measure very small forces where SNR is often not large. Small mechanical and electronic noises together with the laser induced motion might complicate the detection of the force detected NMR signal. Also it is worthwhile to note the slight suppression and enhancement of the Brownian amplitude for blue and

²The absolute value of the slope on both sides of the fringe are the same. If the absolute value of the slopes were different, that would explain the difference in the amplitudes. See Section 2.4 for details.

³Decrease in the resonance frequency, $\omega_0 \sim k^{1/2}$ can be attributed to a decrease in the spring constant as a result of softening the cantilever due to temperature elevations.

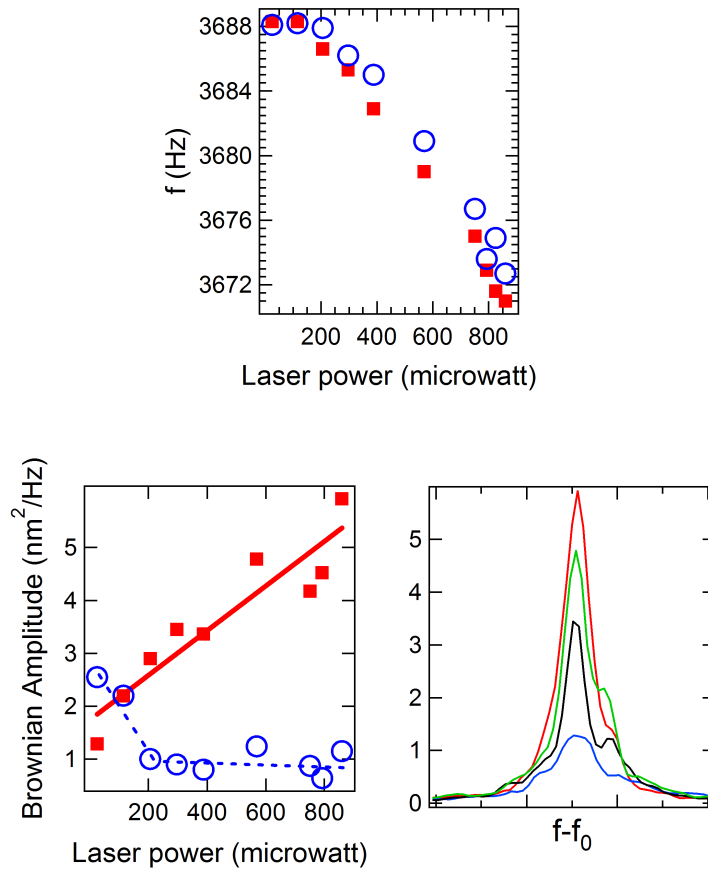


Figure 3.3: Resonance frequency (top) and Brownian amplitude (bottom left) versus the laser power incident on the cantilever for both red detuning (squares) and blue detuning (circles). Some of the Brownian curves obtained for red detuning of the cavity.

red detuning respectively as shown in Figure 3.3b. The enhancement of Brownian noise must not be confused with self oscillation because we have not observed self oscillation that can sustain itself for this cantilever up to laser powers of 1 mW at cantilever.

When tuning of the cavity is enhanced by making sure the cantilever and fiber are parallel and also by reducing the transmitted light through the cantilever by using slightly thicker 570 nm cantilevers, we observe self sustained oscillation above a threshold value of the laser power of 300 μ W (Figure 3.4). The frequency of the self-sustained oscillation was verified to be at the cantilever's resonance frequency using the spectrum analyzer.

Our current understanding of this phenomenon involves a combined driving of the cantilever via both the radiation force and thermal heating. When the cavity, consisting of faces of fiber and cantilever, is detuned, the cantilever will experience a radiation force⁴, pushing it back. However, without a nonlinear term this instantaneous force will not drive the cantilever. The origin of the nonlinear driving force is thermal heating of the cantilever that softens (reduced spring constant) the cantilever. This softening will indeed allow the cantilever to move away from the optical fiber under radiation pressure. Since the cantilever repositioned itself in such a way that the incident power is less this will cause the cantilever to cool and stiffen, and the cantilever will move toward the fiber against radiation pressure. The most important point here is that radiation force alone or thermal softening by itself will not drive the cantilever. Blue detuning of the cantilever acts as a negative feedback.

To summarize, we have argued that self-sustained oscillations are induced by the coupling of the nonlinear heat diffusion effect to the radiation pressure exerted on the single crystal silicon cantilever. Metal-coating or growing additional oxide

⁴Force exerted by radiation pressure is not very small, $F_{rad} = P/c \simeq 10^{-12}$ N compared to the weight of this particular cantilever $W = mg \simeq 3 \times 10^{-12}$ N. The thermal force for this lever is $F_{min} \simeq 10^{-15}$ N.

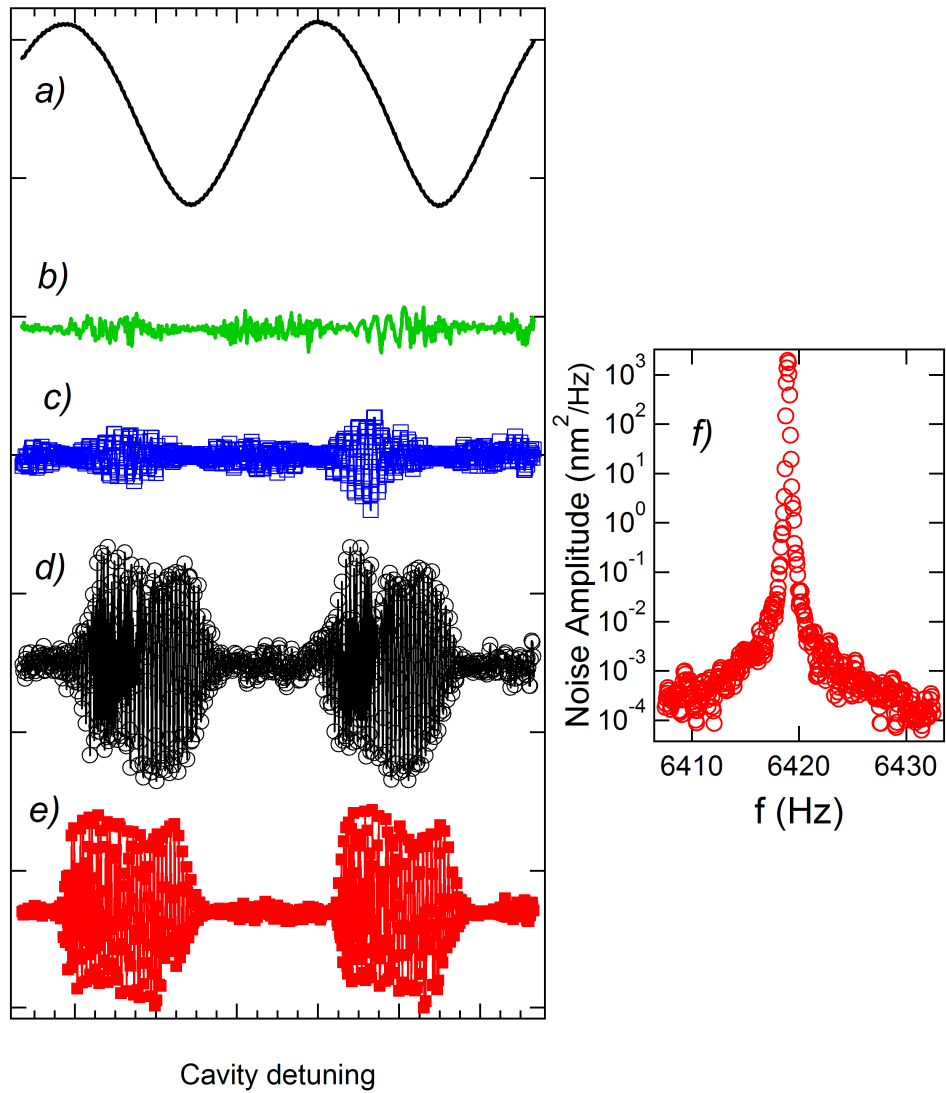


Figure 3.4: a) Interference fringe obtained by ramping the cavity width along with the displacement of the cantilever for b) $240 \mu\text{W}$, c) $300 \mu\text{W}$, d) $390 \mu\text{W}$, e) $960 \mu\text{W}$. f) Fourier Transform of the noise obtained at the red detuning of the cavity. Note the many orders of magnitude of the ordinary.

layers to induce the self oscillation might introduce interface friction thus reducing mechanical Q . The self-oscillation phenomenon may be useful; for example, the effect can be used to drive highly symmetric torsional cantilevers that usually do not effectively couple to the linear drive of piezo actuators.

Chapter 4

Effects of External Field on Torsional Oscillators with Micromagnets

Micromagnets on cantilevers are essential when using the MRFM technique in scanning mode to image small scale features of the sample. The magnetic gradient from a micron scale magnet attached to a cantilever will couple to the nuclear moments of the sample. The small size magnets can produce large gradients thus reducing the thickness of the resonance slice and increasing the magnetic force. Cantilevers with micromagnets placed in the external magnetic field will be affected by the coupling of the external field to the micromagnets. So groups using micron size magnets on cantilevers for MRFM characterize them for their experimental configuration [32], [33]. In order to study the coupling between the external field and micro-magnets mounted on double torsional oscillators, we have extended our prior thin-film micromagnetometry measurements to much smaller magnets [34]. In addition to quantitative measurements of the magnetic moment and magnetic anisotropy of our micromagnets, we determined both the effect of oscillating the magnets in

	A		B	
	f_0 (kHz)	Q	f_0 (kHz)	Q
Lower Cantilever	24.9	6700	5.56	6500
Upper Cantilever	53.1	5500	9.9	10500
Lower Torsional	135.1	12000	29.6	6700
Upper Torsional	160.8	7200	49.9	7300

Table 4.1: The resonance frequencies and quality factors of four major oscillation modes of our two double torsional oscillators (see text for more information).

an external magnetic field on the resonant frequency and on the Q values of the oscillators. Such determinations are required to properly model the behavior of our micromagnets during NMRFM experiments. For these studies we used an earlier generation of single-crystal silicon double-torsional oscillators (Figure 4.1); these had a thickness of ~ 500 nm and other design considerations (note the long oscillator necks in Figure 4.1) to maintain low resonant frequencies for NMRFM. Oscillators with two different magnets will be discussed; Oscillator A has a $15\mu\text{m} \times 15\mu\text{m}$, 30-nm-thick and Oscillator B has a $3\mu\text{m}$ -diameter, 180-nm-thick Permalloy ($\text{Ni}_{80}\text{Fe}_{20}$) magnet.

Although several other oscillation modes [22] were observed, we limited this study to only the four major oscillation modes discussed above: the lower (symmetric) and upper (antisymmetric) cantilever and torsional modes, as shown in Figure 4.2. To determine the resonant frequencies, the oscillators were glued with GE7031 varnish to a piezoelectric plate that was shaken by an applied sinusoidal voltage¹.

The resulting motion of the oscillator was detected by a fiber optic interferometer; the zero-field resonant frequencies detected and the Q -values are given in Table 4.1. Phase sensitive detection on the right and the left sides of the head and wing was used to identify the resonant modes of the oscillator. These measurements

¹The reason for not using the superglue as it has been used for other studies discussed in this work is that this NMRFM probe was lowered into the superconducting magnet with the sample space temperature sometimes below 220 K. I had problem with superglue or other epoxies cracking and the cantilever chip coming lose.

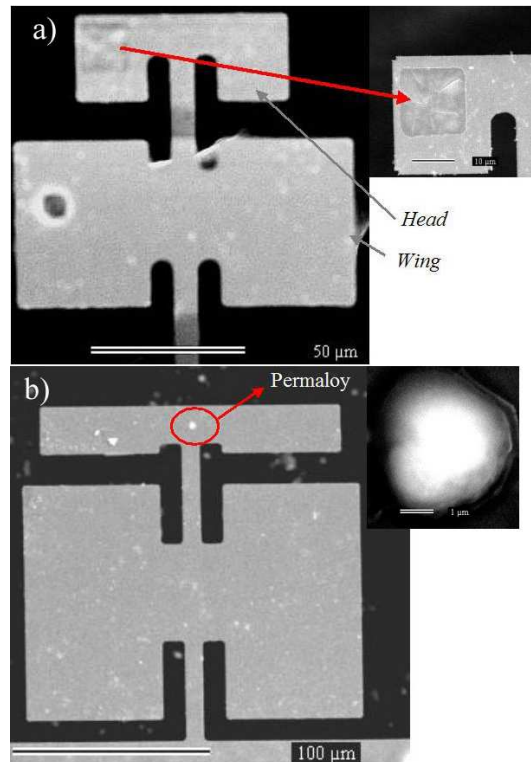


Figure 4.1: Double-torsional micro-oscillators used in the micromagnetometry experiments. Oscillator A on top has a larger magnet ($15\mu\text{m} \times 15\mu\text{m} \times 30\text{nm}$). Oscillator B at the bottom has the smaller magnet ($3\mu\text{m}$ -diameter, 180-nm-thick).

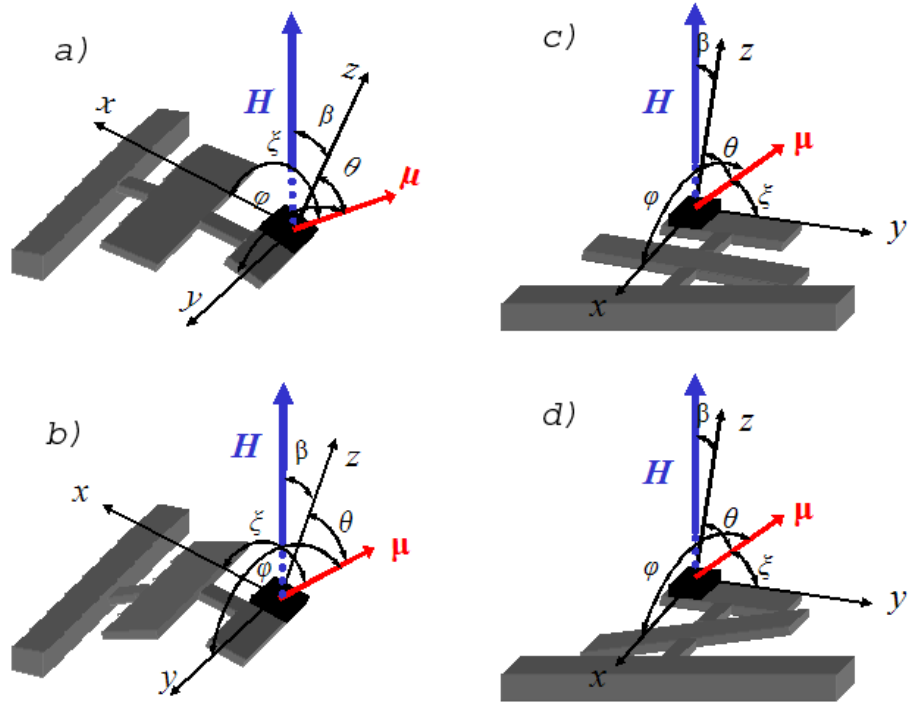


Figure 4.2: The major oscillation modes of our double torsional oscillators, and the geometry used to determine the magnetic energy and equilibrium moment directions. a)The lower cantilever mode. b)The lower torsional mode. c)The upper cantilever mode. d)The upper torsional mode.

were carried out at room temperature and 10^{-5} torr. To investigate the field dependence of the resonant modes, driven frequency scans were performed for several values of an external magnetic field that was applied perpendicularly to the plane of the oscillator (and thus the Permalloy film); this is the geometry appropriate for the NMRFM experiments described below. The field-dependent resonant frequencies and quality factors were obtained by fitting a Lorentzian curves to the driven scans. Our experimental results are shown in Figure 4.3. The frequency shift is normalized to the zero-field resonance of each mode. As previously observed [34], the oscillators exhibit two regimes of field dependence: there is an initial softening at low fields, followed by a stiffening at high fields. Increasing the external field causes the

magnetic moment of the film to rotate from its initial in-plane orientation, due to shape anisotropy, through intermediate orientations, and ultimately into alignment with the field at high field values. Resonant frequencies of the lower and the upper cantilever modes decrease (softening regime) for fields less than a switching field of about 1 T, then increase (stiffening regime) for higher fields. The switching field for the lower and upper torsional modes was found to be about 0.6 T. The resonant frequencies of the upper torsional and cantilever modes exhibit smaller relative field-induced changes than the lower modes; this is because the comparable magnetic torques have a smaller absolute effect at higher frequencies. The field dependence of the resonant frequencies of the four oscillator modes can be understood within a single-domain model of the magnet on the oscillator. The model parameters and geometry we use are given in Figure 4.2, above. We first consider the cantilever modes, and then apply a similar formulation for the torsional modes. Due to shape anisotropy, the easy plane of the magnet is in the axis of the oscillator. The energy functional (up to a constant) for this case can be written as

$$\frac{E}{V} = K_x \sin^2 \xi + K_y \sin^2 \phi - M_s H (\cos \beta \cos \theta - \sin \beta \cos \phi) \quad (4.1)$$

where K_x and K_y are first-order anisotropy constants in the x and y directions, respectively, and M_s is the saturation magnetization. The energy of the system can be minimized with respect to ϕ and θ to find the direction of the magnetic moment of the domain. Using trigonometric identities to rearrange the energy and assuming that the oscillator deflection angle $\beta \ll 1$, we obtain

$$\cos \theta = \frac{H}{H_{k,x}} \quad \text{and} \quad \cos \phi = \frac{H}{H_{k,yx}} \beta \quad (4.2)$$

where $H_{k,x} = 2K_x/M_s$ and $H_{k,yx} = 2(K_y - K_x)/M_s$. The x component of the

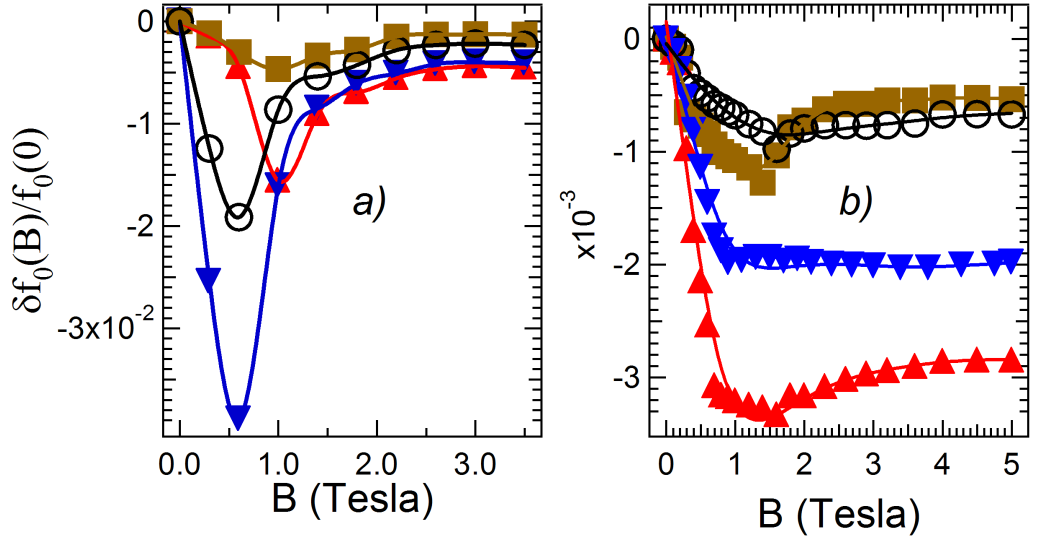


Figure 4.3: Magnetic-field dependent resonant frequencies relative to the zero-field value for oscillator A (large magnet, left panel) and Oscillator B (small magnet, right panel). In each case the modes are: lower cantilever (upward triangles), lower torsional (downward triangles), upper cantilever (squares) and upper torsional (open circles).

magnetic torque is

$$\tau_x = \mu_y H_z - \mu_z H_y = -\mu H^2 \beta \left(\frac{1}{H_{k,x}} - \frac{1}{H_{k,yx}} \right) \quad (4.3)$$

We equate this with the restoring torque², $\tau_x = \Delta k_o \beta L_{eff}^2$ to obtain the frequency shifts $\Delta f_o/f_o = \frac{1}{2} \Delta k_o/k_o$. Here, Δk_o is the spring constant change and L_{eff} is the effective length of the cantilever. For fields H below $H_{k,x}$ this gives

$$\frac{\Delta f_o}{f_o} = -\frac{\mu H^2}{2k_o L_{eff}^2} \left(\frac{1}{H_{k,x}} - \frac{1}{H_{k,yx}} \right) \quad (4.4)$$

At high enough fields, when $H > H_{k,x}$, the magnetic moment approaches the y - z

²Restoring torque, $\tau_x = F_x L_{eff} \beta$, is the result of the restoring force, $F_x = \Delta k L_{eff} \beta$ and this force will effectively change the spring constant of the oscillator.

plane. This results in the special case $\xi = \pi/2$ and $\sin \phi = -\cos \theta$. Our energy then takes the form $E/V = K_y \sin^2 \phi - M_s H - H \cos(\beta - \phi)$, yielding a magnetic torque[32] of the form $\tau_x = \mu H \beta [H_{k,x}/(H + H_{k,x})]$. From this we obtain (for $H > H_{k,x}$)

$$\frac{\Delta f_o}{f_o} = \frac{\mu H}{2k_o L_{eff}^2} \frac{H_{k,x}}{(H + H_{k,x})} \quad (4.5)$$

Equations 4.4 and 4.5 describe the softening and stiffening regimes of the oscillator.

It is worth noting that both the lower and upper cantilever modes have the same transition field between these two regimes. It is not surprising because the resultant magnetic torque in both cases act the same way.

For the torsional modes the same reasoning applies, but we must instead consider the restoring torque about the y axis, $\tau_y = \Delta \kappa_o \beta$, where $\Delta \kappa_o$ is the change in torsion constant. The resulting frequency shifts are identical in form to Equations 4.4 and 4.5, with $H_{k,y} = 2K_y/M_s$, $H_{k,xy} = 2(K_x - K_y)/M_s$, and the torsion constant κ_o substituted for $H_{k,x}$, $H_{k,yx}$, and the product $k_o L_{eff}^2$, respectively. Thus we also see that both the lower and upper torsional modes have the same transition field, and this field is different from that of the cantilever modes³.

Since the relative frequency shift of a cantilever (torsional) mode is inversely proportional to the spring (torsional) constant, such shifts are smaller for the higher frequency modes, as is evident in Figure 4.3. For our oscillators with parameters $L_{eff} \approx 100\text{--}150 \mu\text{m}$, $k_s \approx 0.01\text{--}0.030 \text{ N/m}$, and $\kappa_o \approx 6.0 \times 10^{-10} \text{ N}\cdot\text{m}$, the fits to Equations 4.4 and 4.5 are shown in Figure 4.4. The fits provide a moment measurement for the larger magnet of Oscillator A of $\mu = 4.6 \times 10^{-12} \text{ J/T}$, in agreement with the value $\mu = 4.5 \times 10^{-12} \text{ J/T}$ from the estimated volume and the permalloy saturation magnetization value of 670 kA/m. For the smaller magnet of Oscillator B, the extracted moment is $8.3 \times 10^{-13} \text{ J/T}$, in fair agreement with the value

³The magnetic torque experienced for both lower and upper torsional modes is the same but different from cantilever modes

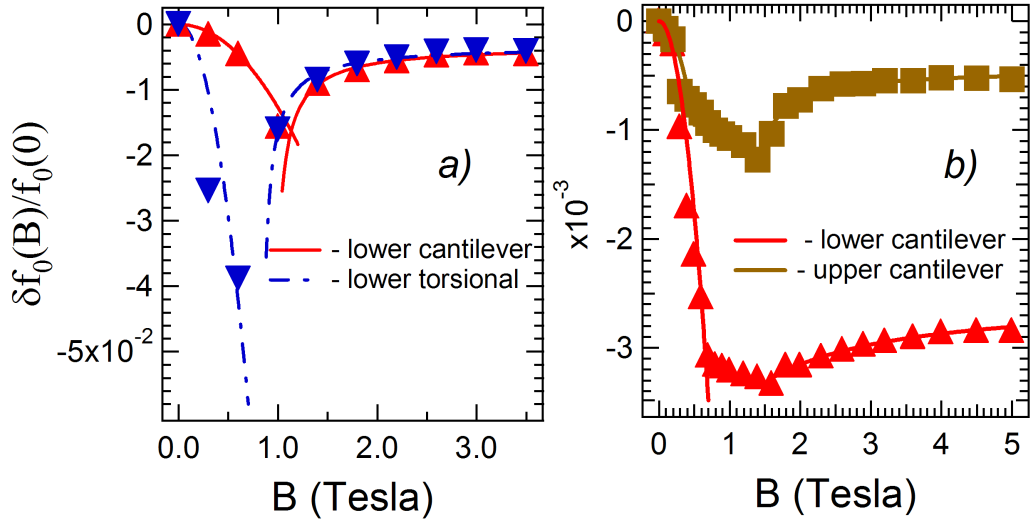


Figure 4.4: Fits to the low-field and high-field regimes of the field-dependent mechanical oscillator resonant frequency, using Eqs. 4.4 and 4.5.

1.1×10^{-12} J/T, calculated with appreciable volume uncertainty. The extracted anisotropy fields for the larger magnet are $H_{k,x} = -0.83$ T and $H_{k,y} = -0.80$ T; these are nearly equal, as expected from the nearly square shape; for the smaller magnet, the values are $H_{k,x} = -0.60$ T and $H_{k,y} = -0.87$ T, reflecting the more irregular shape of the smaller magnet.

On a final note, this study also shows that magnetic moments obtained by torque measurement have sensitivity of an order $\sim 10^{-12}$ J/T that is 1000 times better than the sensitivity of the commercially available SQUID magnetometers. The behaviour of Q at high field seems very promising for micromagnet on cantilever to be used in NMRFM since Q value does not degrade at high field where most NMRFM probes operate. However, the empirical observation of the fact that the quality factor of the oscillator experiences damping around the field value where the magnetic moment of the micron size thin film changes the orientation from in plane to out of plane direction must be noted (Figure 4.5).

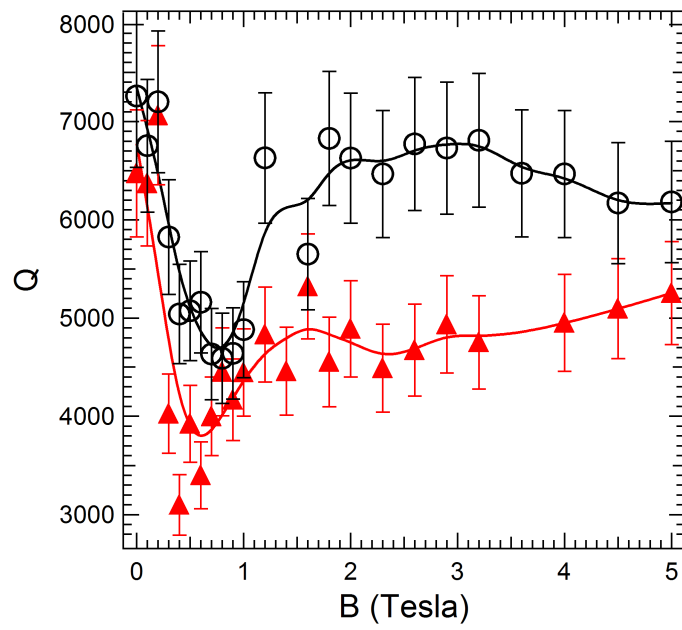


Figure 4.5: Quality factor as a function of field for the lower cantilever mode of Oscillator A (triangles) and Oscillator B (circles). Lines are guides to the eye.

Chapter 5

Results and Discussion

5.1 Experimental Parameters

As mentioned before, the sample of choice for our experiment was ammonium dihydrogen phosphate (ADP). It is a well suited sample for our purpose since it has a high proton density, $n = 5.7 \times 10^{10}$ protons/ μm^3 , it is easily available, and it is inert under the ambient conditions. The $80 \times 80 \times 60 \mu\text{m}^3$ sample was glued to the oscillator as shown in Figure 2.21. T_1 and $T_{1\rho}$ for ADP has been well characterized by means of conventional NMR [35], [36]. Around room temperature, these values are long enough for sampling with the cyclic inversion scheme (Figure 5.1). Also some cooling below the room temperature provides access to T_1 and $T_{1\rho}$ values at temperatures below the T_1 minimum, and warming above the minimum provides variations in T_1 in the short correlation time regime.

The next two sections describe the experimental parameters used for each of the measurements.

One thing we must note is that the reading from the Gaussmeter is 500 to 900 Gauss larger than actual field setting. The offset is usually very stable once the Gaussmeter is turned on. This requires a recalibration of the resonance conditions

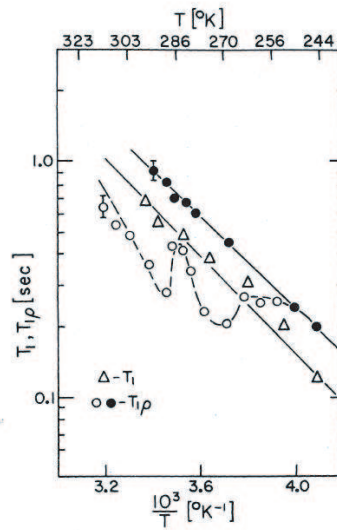


Figure 5.1: $T_{1\rho}$ data for ADP in the vicinity of room temperature shown for both unannealed (open circles) and annealed samples (closed circles). The triangles indicate the T_1 values, which do not depend on annealing. Ref. [35].

every time the field and Gaussmeter are turned on.

5.2 Detection of the NMRFM signal from ADP sample

Table 5.1 summarizes the experimental conditions used for a 1-D imaging scan of the ADP sample that will be discussed here.

Exp. Parameters	Values
f_{osc} (kHz)	1.45
Q	600
k (N/m)	0.02
Ω (kHz)	100
B_1 (mT)	$\sim 20 \pm 5$
$\nabla_z B_y$ (T)	300

Table 5.1: The experimental parameters used for imaging the ADP sample.

Here we will outline the basic calculations we have done to estimate the antic-

ipated force on an oscillator due to the interaction of the nuclear magnetic moment with the applied field gradient. For the parameters given in Table 5.1, the relation $\Delta z = (2\Omega/\gamma)/(\nabla_z B_y)$ provides a $17\mu\text{m}$ thick resonance slice. An active sample volume of $80 \times 80 \times 16 \mu\text{m}^3$ yields a magnetic moment of $\mu = [nV(\gamma\hbar)^2 B_0]/(4k_B T) = 3.25 \times 10^{-16} \text{ J/T}$. The resulting force on the oscillator shown in Figure 2.21 is $F_z = \mu_z \nabla_z B_y = 9.7 \times 10^{-14} \text{ N}$. It is 8.3 times the thermally imposed minimum detectable force, $F_{min} = 1.2 \times 10^{-14} \text{ N}$. These numbers look very optimistic.

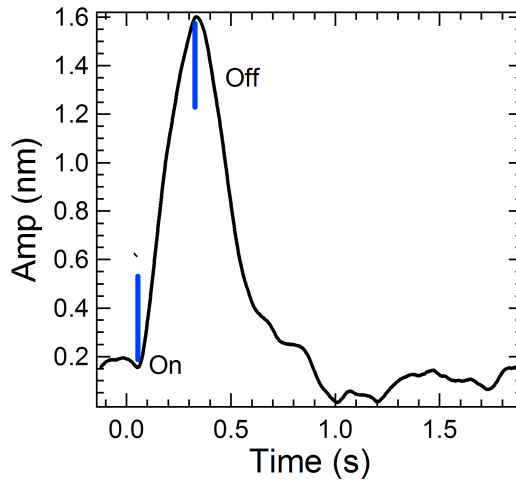


Figure 5.2: Magnitude of the cantilever's response for NMRFM experiment. The cyclic inversion time is 300 ms and the lock-in time constant is 100 ms. The shown curve displays the magnitude of the measured signal with the background spurious excitation subtracted, and is an average of four measurements. This measurement produced the data point at $B_0 = 15100 \text{ G}$ for the 53.7 MHz curve in Figure 5.3.

Our experimental setup is shown in Figure 1.7. I swept the field in steps of 50 gauss¹. The motion of the oscillator is enhanced due to magnetic resonance when the resonant slice enters the sample (see Figure 5.3). The resonance condition corresponding to the set carrier frequency will result when the sum of the external field and the field due to the iron sphere match the Larmor frequency. The peaks in

¹50 G steps correspond to $17 \mu\text{m}$ steps of the resonance slice.

Figure 5.3 occur when the resonance slice contains the largest amount of the sample. I have performed field sweeps for two different carrier frequencies, 52.7 MHz and 53.7 MHz² (Figure 5.3). The observed shift of the NMR peak confirms that the nuclear spins of the sample are responsible for the force on the oscillator.

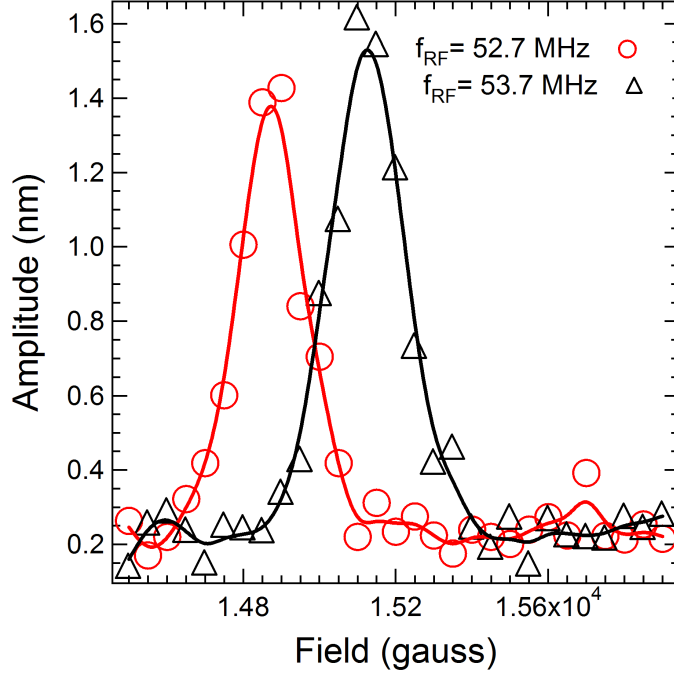


Figure 5.3: Peak amplitude of cantilever response versus field for two different carrier frequencies separated by 1 MHz. Each point represents an average of four measurements.

The peak value of the oscillation amplitude of the oscillator is 1.6 nm at 53.7 MHz, giving a measured force of $F_{meas} = kA/Q = 5.3 \times 10^{-14}$ N. This agrees roughly with the expected value of $F_{exp} = 9.7 \times 10^{-14}$ N. The fact that the measured force is less than expected may be attributed to the fact that during cyclic inversion the effective field does not fully invert spins from the $-z$ to $+z$ direction, but only $\phi = \arctan((\Omega/\gamma)/B_1) = 50^\circ$. This effect is discussed in more detail in the next

²These correspond to a field value of 1.237 T and 1.261 T, respectively.

section.

5.3 Characterization

In this section we will see how the force detected signals of nuclear moments depend on some of the parameters used in NMR-FM. Again the summary of the experimental details is given in the Table 5.2.

Exp. Parameters	Values
f_{osc} (kHz)	1.23
Q	400
k (N/m)	0.02
$\nabla_z B_y$ (T)	300
f_0 (MHz)	52.7

Table 5.2: Experimental parameters.

Since the sample I am using is quite thick, $\sim 70 \mu\text{m}$. increasing the thickness of the resonance slice, $\Delta z = (2\Omega/\gamma)/\nabla_z B$ while keeping the field gradient unchanged should increase the signal due to the increase in the amount of nuclear magnetization sampled. Figure 5.4 illustrates the fact that the thickness of the resonance slice is somewhat linear with the modulation amplitude. Also, changing the strength of the RF field enhances the signal. If we carefully consider what happens to the maximum magnetic moment in the z direction, given by:

$$(\mu_z)_{max} = \frac{\mu_0}{\sqrt{1 + (\gamma B_1/\Omega)^2}}, \quad (5.1)$$

we quickly realize that magnetization in the z direction is getting smaller with the increasing field. However in our case it is quite contrary (Figure 5.4). In order to effectively manipulate most of the nuclear spins the RF field must be strong. It is generally true for solids that the value of B_1 must be bigger than the local moments seen by nuclei. Thus increasing the RF field will increase the amount of nuclei in the

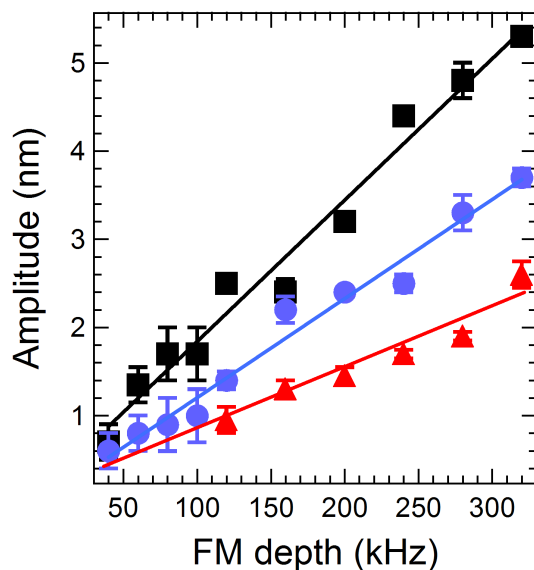


Figure 5.4: The vibration amplitude of the oscillator with the ADP for 19 Gauss (■), 15 Gauss (●), 10 Gauss (▲) versus frequency modulation amplitude. All the measurements were done on resonance. Each data point represents the average of 16 cyclic inversion measurements.

resonance slice grabbed during the cyclic inversion, and this results in enhancement of the force detected signal.

The adiabatic condition for sinusoidal cyclic inversion, $\Lambda = (\gamma B_1)^2 / (\omega_{osc} \Omega) \gg 1$, determines how well the nuclear spins are locked to the effective field as mentioned in Section 1.2. If the adiabatic condition is not fully satisfied, the nuclear magnetic moment will decay during the cyclic inversion. Figure 5.5 illustrates what happens when the modulation amplitude is kept constant but B_1 is varied. When the RF field is reduced we observe that the cantilever amplitude decays during the cyclic inversion, meaning that a decay in the magnetic moment locked to the effective field is causing the decay in magnetic force experienced by the cantilever. Table 5.3 shows the calculated values for the adiabatic factors Ω for each of the sweeps in Figure 5.5. These values are consistent with those found in a recent study [31]

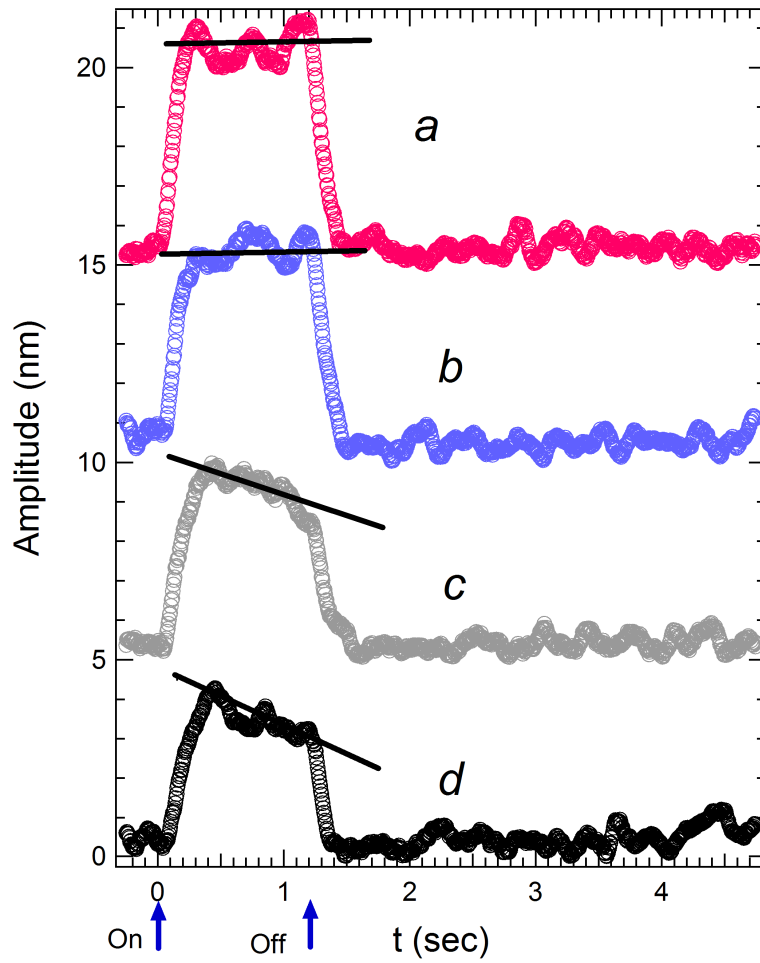


Figure 5.5: Cyclic inversion with RF field of a) 15 Gauss, b) 11 Gauss, c) 9 Gauss and d) 7 Gauss and the amplitude of FM is 280 kHz Duration of the inversion is 1.2 s, start and end times are indicated by the arrow. Each of these graphs is the result of 16 averagings.

The decay in magnetization cannot be completely attributed to poor spin locking. The longitudinal decay of the magnetization that is determined by $T_{1\rho}$ during the cyclic inversion also occurs more quickly with decreasing RF field, and so may also be partly responsible for signal decay.

B_1 (G)	$(\gamma B_1)^2/(\omega_{osc}\Omega)$
7	2.55
9	4.23
11	6.38
15	11.9

Table 5.3: Adiabatic factor versus FM RF field. Amplitude of the modulation is 280 kHz.

5.4 Spin Manipulation with Pulses

In this section I will demonstrate the effect of the pulse on the net magnetization of the sample in the resonance slice. We apply a short on-resonance pulse and then use the modulated RF field to sample the magnetization as shown in Figure 2.18b. The experimental parameters for this measurement are given in the Table 5.4.

Exp. Parameters	Values
f_{osc} (kHz)	1.23
Q	400
k (N/m)	0.02
$\nabla_z B_y$ (T)	300
f_0 (MHz)	52.7
Ω (kHz)	100

Table 5.4: Experimental parameters.

During the measurement the wait time between the first short on-resonance pulse and the modulated RF field used for sampling is 15 ms. Figure 5.6 shows the experimental results when the pulse width was varied between 0 to 21 μ s.

This results represents a so-called spin *nutaton* experiment. With the help of the pulse the magnetization is rotated in a plane perpendicular to B_1 by an angle $\theta = \gamma B_1 t_{pulse}$ as described in the Section 1.1. The power of the RF pulse was 38 dBm and the power of the sampling field was 33 dBm³.

The data points were fit to $\exp(-t_{pulse}/\tau) \cos(\gamma B_1 t_{pulse}) + C$. The values

³The RF power was sent to the *LRC* circuit tuned to 50 Ω .

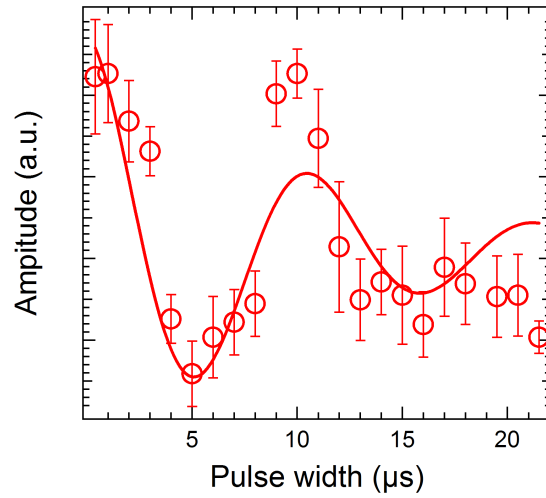


Figure 5.6: Spin nutation data obtained by varying pulse width and sampling the magnetization for 600 ms with the cyclic inversion scheme. The wait time between the pulse and the sampling is 15 ms.

extracted from the fit are $B_1 = 22 \pm 1$ Gauss and the $\tau = 10 \pm 2\mu\text{s}$. The decay of the magnetization can be attributed to the dephasing of the magnetic moments in the transverse direction in a sample due to homogeneous spin-spin interactions and to the inhomogeneous field.

Chapter 6

Magnetism In Cobalt Nanocrystals

In this chapter I will briefly describe another project that deals with magnetic nanocrystals and is not entirely motivated by MRFM. However these nanoscale magnetic systems one day can be used as nanomagnets on cantilevers and it is worth studying them. They are also very interesting model systems that can improve our understanding of microscopic magnetism. They are also very appealing from an applicational point of view.

6.1 Motivation

Reducing the size of magnetic particles gives rise to many novel magnetic properties [37], [38], [39]. Up until recently the main challenges that kept these magnetic nanoclusters from being utilized in magnetic recording media was their random size and orientation and their non-uniform magnetic properties. To make recording feasible, it is very important that the material has uniform magnetic properties over a large area. The revived interest in magnetic nanostructures came with the break-

through observations of fairly uniform ferromagnetic properties for various quantum grown nano-assemblies. These assemblies also demonstrated enhanced anisotropy energy per magnetic atom that quickly degrade with the size of the particle [40]. This limits the blocking temperature of the nanoparticles. Long range dipole interactions in a densely grown particle system can contribute to the collective behavior of the particle system and increase the Curie temperature above the superparamagnetic limit of the single particle [41]. There have been successful attempts to grow nano-dot assemblies with the high Curie temperature that is induced through the substrate coupling [42]. Self assemblies utilizing conducting substrates introduce substrate hybridization into magnetic nanostructures. The long term prospects for industrial applications would be to either decrease or completely avoid the collective behavior of the particles and still maintain ferromagnetic properties at easily achievable environments. Blocking temperature can also be increased by stabilizing magnetization with the exchange bias [43].

In this chapter I will show the systematic magnetic measurements and observations of self assembled cobalt nanocrystals grown on a Si(111) substrate. Enhancement of the anisotropy energy and the magnetic moment for the cobalt atoms in the nanocrystals that consists of 350 atoms was explored within the framework of the single domain model. We will see that dipolar and substrate-mediated interactions that are responsible for enhancement of Curie temperatures in many systems of nano-assemblies can be ruled out for our system.

6.2 Sample Preparation

Sample preparation and Scanning Tunneling Microscopy (STM) imaging were carried out in Ultra-High Vacuum conditions ($< 5 \times 10^{-11}$ torr). The STM images were recorded at room temperature in constant current mode. Clean Si (111) substrates (p-doped, with a resistivity of 3-5 $\Omega - \text{cm}$) were prepared using well-established

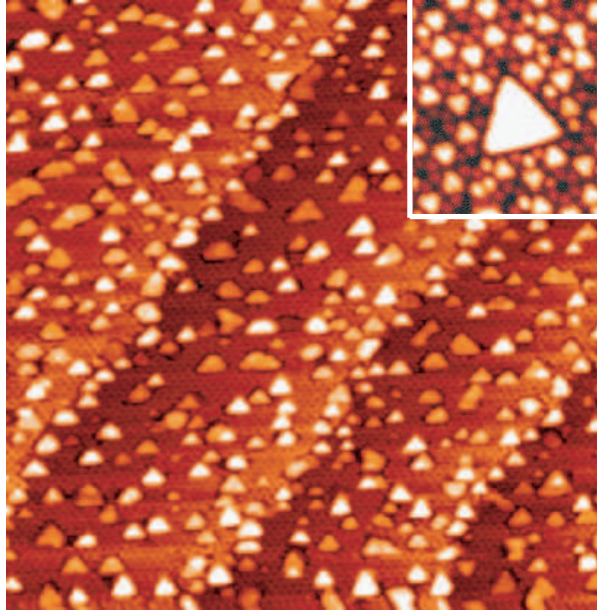


Figure 6.1: $120 \times 120 \text{ nm}^2$ STM image of self assembled equilateral Cobalt nanocrystals with the side dimensions of 5.5 nm and a 2ML height on top of Si (111). Inset shows an enlarged image of one of these Cobalt nanoplatelets. Tiny clusters in the inset are Al templates of 6 atoms each occupying half of the 7×7 unit cell.

annealing procedures. Co deposition was carried out by direct-current heating of a tungsten filament coated with Co. The deposition rate was approximately 0.1 ML/min ($1 \text{ ML} \sim 7.8 \times 10^{14} \text{ atoms/cm}^2$). Before Co deposition, we utilized a recently discovered self-assembly approach to prepare a template consisting of the Si (111) substrate covered by a spatially ordered and identically sized Al cluster array [44], [45]. The Al layer acts as a protecting layer to prevent silicide formation, and the Al layer and Si substrate serve as a template to form uniformly sized Co platelets as shown in Figure 6.1. Each particle consists of roughly 350 cobalt atoms. We deposited a 10 nm-thick Au layer onto the samples to avoid oxidation during

sample transportation. We chose gold as a capping material because coating the nanocrystals with gold should not affect the magnetic properties of cobalt atoms [47], [48].

6.3 Magnetic Measurement and Analysis

The precise size and dilute distribution of particles in the system determines the uniform magnetic properties across the whole silicon substrate. This allows the use of global measuring techniques for direct measurement of magnetic properties. We used a Quantum Design MPMS SQUID for these magnetic measurements. By measuring hysteresis curves for fields applied in plane and perpendicular to the plane of the substrate we found that the easy axis of magnetization is out of the plane. The hysteresis curves in Figure 6.2 show that coercive fields of ~ 220 Oe and ~ 160 Oe are observed at 5 K and 70 K respectively.

Both hysteresis curves reach saturation at approximately 5000 Oe, which suggests that these cobalt nanocrystals are behaving as non-interacting single domain particles. Another interesting observation is the reproducible jiggle seen in the hysteresis curves at around 2000 Oe prior to reaching the coercive field. The reason for these jiggles is non-uniform coverage due to small amounts of nanocrystals that are very close to each other and give rise to magnetic pinning through the dipolar interaction exhibited in low field instabilities¹. However, for the most part our substrates contained uniformly spaced nanocrystals.

Various densities of particles from 0.2 up to 0.5 ML coverage (10 and 25 percent areal coverage) were studied for the N=2 nanocrystals. In Figure 6.3 we show both the coercive field and the remnant moment as a function of temperature for 15 and 25 percent areal coverage.

¹The dipolar field from the center of one platelet at 10 nm distance is roughly 6 G. For particles in densely packed areas the total dipolar field gets sufficiently large. For simplicity, each nanocrystal is assumed to be point source.

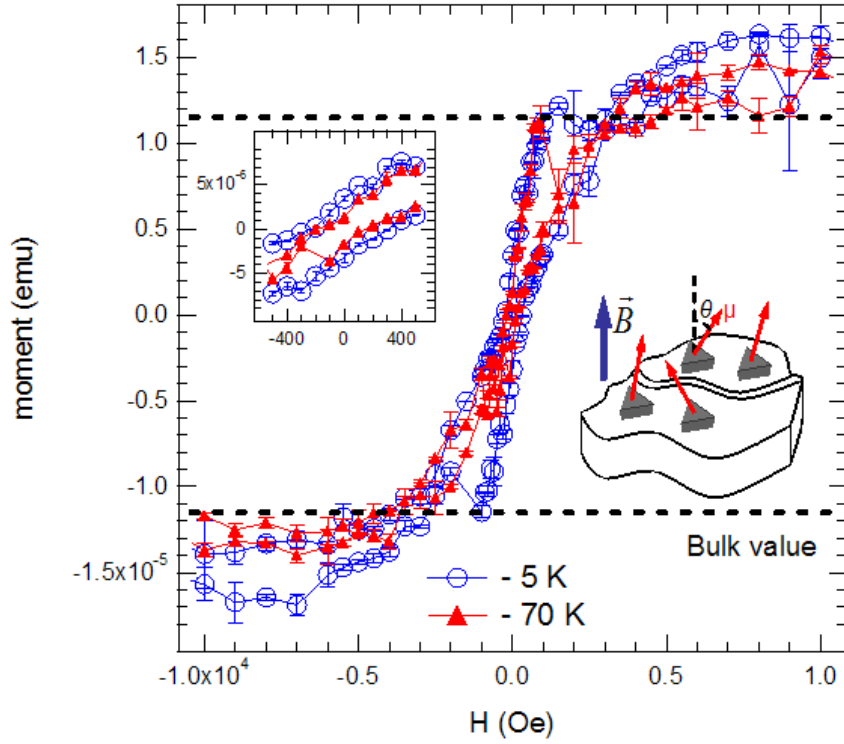


Figure 6.2: Hysteresis curves for a sample with 50 percent aerial coverage obtained at 5 and 70 K with the field applied perpendicular to the surface of the substrate. Inset shows an enlarged image of the hysteresis curve.

The weak dependence of blocking temperature to the density of particles suggests that inter particle coupling does not play any role on the ferromagnetic order. Inter particle dipolar interactions can be ruled out because of the low platelet density of our samples. Substrate mediated indirect coupling is unlikely on a passive Si(111) substrate compared to other substrates where it has been demonstrated that surface plays an important role for particle interaction [42]. The so called blocking temperature, T_B , that describes the transition between ferromagnetic and superparamagnetic phases is given by the Boltzmann relation,

$$\tau = \tau_0 e^{KN/k_B T_B} \quad (6.1)$$

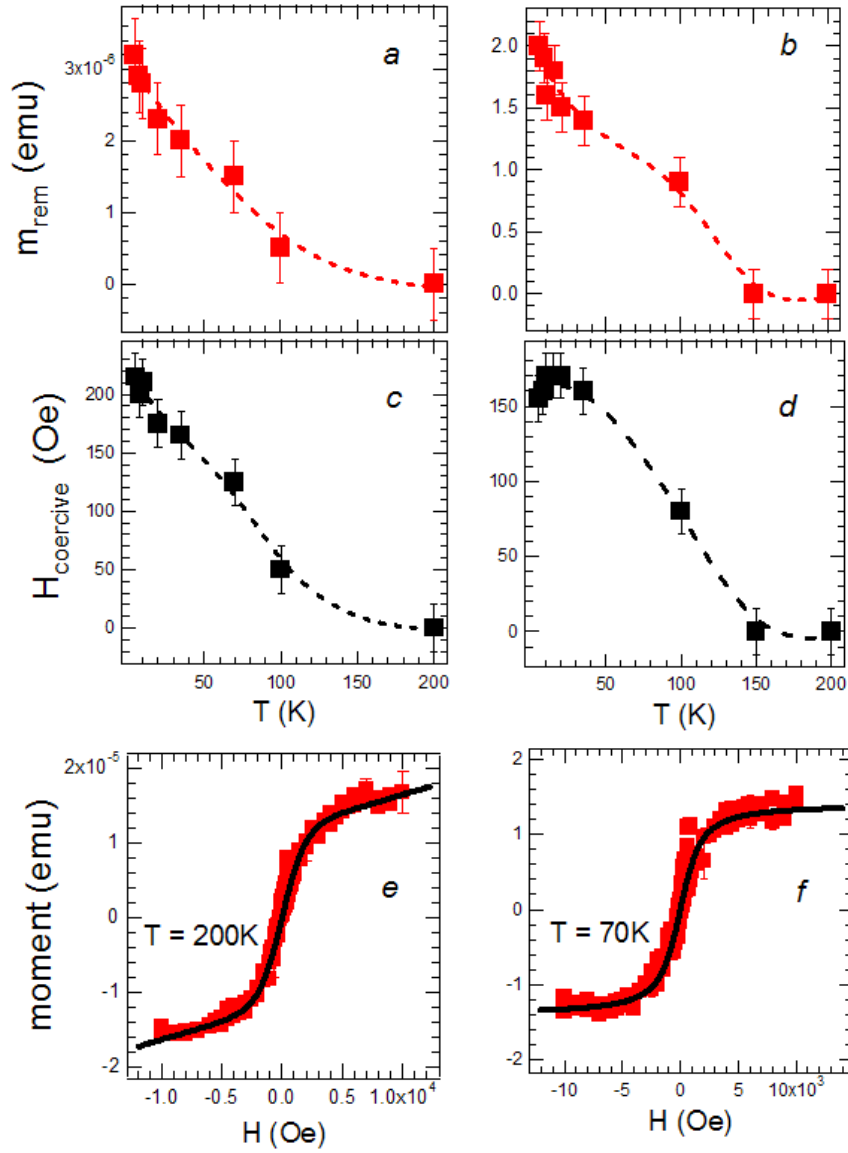


Figure 6.3: (a) and (b) are the remnant moments of the systems with 25% and 15% areal coverage. (c) and (d) are the coercive fields of the systems with 25% and 15% areal coverage. For both samples superparamagnetic behavior sets in above 100 K. Dashed lines are guides for the eyes. (e) and (f) represent hysteresis curves fitted to the single domain model for a sample with 25% coverage at 200 K and 70 K (solid lines) above the blocking temperature, T_B . See the text for details.

where $\tau_0 = 10^{-9}$ sec, $\tau \sim 10^2$ sec is a typical measurement time, K is the anisotropy energy per atom and N is the number of atoms per platelet [49]. The blocking temperature for both samples is around 100 K. We estimated an anisotropy energy to be ~ 0.62 meV per cobalt atom from [37].

The size and shape of the particles for both concentrations are identical, which makes sense considering a model of non-interacting single domain nanoclusters [39]. Using Boltzmann's distribution, we can write down the expression for the moment of an ensemble of single domain particles, where the external field is applied along the easy axis:

$$M = M_{sat} \frac{\int_0^\pi \cos \theta e^{-N(-K \cos^2 \theta - \mu B \cos \theta)/k_B T}}{\int_0^\pi e^{-N(-K \cos^2 \theta - \mu B \cos \theta)/k_B T}} \quad (6.2)$$

Here, θ is the angle between the easy axis and moment and μ is the moment per particle. We fit this function to our hysteresis curve to obtain μ , K and M_{sat} . The increase in anisotropy energy and magnetic moment compared to the bulk value is obtained from fitting the M-H curve at 200 K and 70 K for the sample with the areal coverage of 25% as shown in Figure 6.3 (e, f). The values of the moment and anisotropy energy are $\mu = 2.1 \pm 0.2 \mu_B$ and $K = 0.45 \pm 0.15$ meV per Cobalt atom, respectively. The enhancement of the Cobalt moment over the bulk value extracted from the fit is in agreement with the saturation moment of the hysteresis curves in Figure 6.2. The reasonable agreement between the anisotropy energy obtained from the single domain model and the blocking barrier in the Boltzmann relation suggests that inter platelet interactions over the whole sample do not make any appreciable contribution to the blocking temperature. This is not surprising considering the fact that substrate mediated interactions are unlikely due to the passive Si (111). The dipolar interactions of our low dilute system are small over the whole sample. By ruling out all the significant magnetic interactions of each nanocrystal with the surroundings, we conclude that enhancement of the magnetic

moment and anisotropy energy seen in the hysteresis curves and obtained from the fit is an intrinsic property for the nanocrystals. It is also interesting to note that increasing the density of nanocrystals will eventually cause them to merge together and form large islands of random height. These islands are magnetic but do not possess any novel properties of cobalt nanocrystals, on the contrary they behave as thin films with an in-plane easy axis.

An aluminum template not only passivates silicon dangling bonds thus stopping silicide formation and allowing cobalt atoms to move freely to self assemble nanocrystals but also slightly enhances the magnetic moment of cobalt atom at the cobalt-aluminum interface. As we mentioned earlier, previous reports indicate only negligible hybridization at the gold-cobalt interface and a moment of $2.1\mu_B$ per Co atom [47]. For our 2 ML tall platelets the magnetic moment is $2.0 \pm 0.1\mu_B$ per Co atom at the Al template Co nanocrystal interface. By comparing our results to earlier works done on free cobalt clusters([51], [52]), we made the significant observation that the moment per cobalt atom in a nanocrystal is comparable to the moment of free cobalt atoms in free nanoclusters. It is well known that the crystalline structures of materials are responsible for its magnetic properties [52]. Here we demonstrate that crystal structure of self assembled nanocrystals will allow us to achieve enhanced magnetic moment and anisotropy energy per Co atom.

In conclusion, we have shown that Co nanocrystals grown on top of silicon with an Al template buffer layer do not form silicide and thus preserve their magnetic properties. We have also shown that based on our ex-situ measurements, the self assembled cobalt nanocrystals have high anisotropy energy with the easy axis perpendicular to the substrate plane. The magnetic moment of an individual cobalt atom in a nanocrystal was enhanced compared to the bulk value. The interactions between nanocrystals were ruled out for relatively dilute density ($< 25\%$ aerial coverage). All of these qualities make the cobalt nanocrystals very promising

candidates for magnetic storage with 100 Tbit/in² density and for implementation into silicon devices. Performing first principle numerical calculations in a system with 350 atoms is well within the capabilities of today's computers. This makes the single domain cobalt nanocrystals highly interesting model mesoscopic systems that will stimulate theoretical understanding of itinerant magnetism.

6.4 Is Single Nuclear Spin Detection Possible?

High spatial resolution with MRFM requires high field gradients. In order to increase resolution smaller and smaller magnets must be used. The smallest magnets on cantilevers today are typically bigger than 1 μm in size. Using a cobalt nanocrystal as the micromagnet would enhance the sensitivity to the point that will be necessary for single nuclear spin detection. Assuming a cobalt nanocrystal to be a single dipole centered in the middle of an equilateral triangle we can calculate the field and field gradient as shown in Figure 6.4.

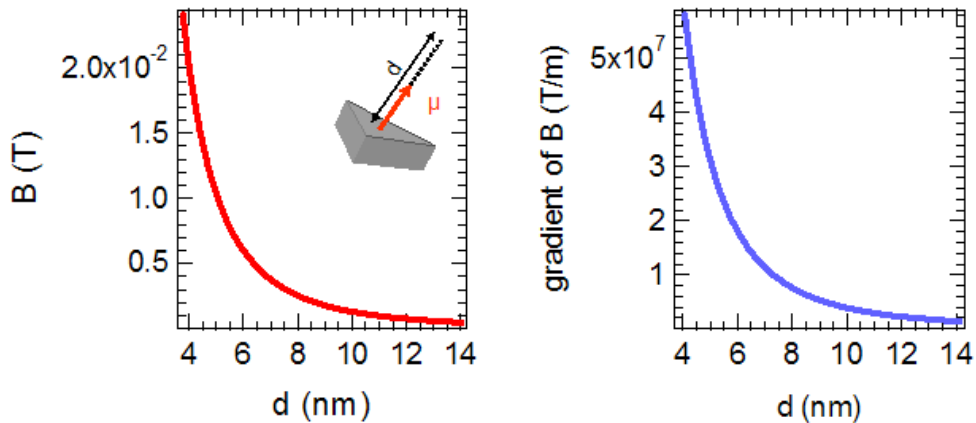


Figure 6.4: Field (left) and field gradient (right) along the easy axis of magnetization versus the distance from the surface of the nanocrystal.

The value of the field gradient is 3×10^7 T/m at a distance 5 nm away from

the sample. For modulation depth, Ω , of 50 kHz this yields a 0.8 Å thick resonance slice. The nearest neighbor distance between two atoms in any crystal is bigger than 1 Å thus making single nuclear spin detection possible.

To estimate the SNR for single nuclear spin detection with the nanomagnet on oscillator setup we utilize state-of-the-art parameters of today's cantilevers: $k = 10^{-5}$ N/m, $Q = 10^5$ and $f_0 = 10$ kHz and $T = 300$ mK, which can be achieved inside a ^3He probe. Using Equation 1.6 we get the minimum detectable force equal to $F_{min} = 1.6 \times 10^{-19}$ N. The force experienced by a single proton is $F = \mu_N \cdot \partial_z B \simeq 4 \times 10^{-19}$ N. This result is very promising, however we should keep in mind that single nuclear sensitivity does not mean straight forward single nuclear spin detection. The rms fluctuation of the cantilever subject to the above conditions $\sqrt{\langle x^2 \rangle} = \sqrt{k_B T/k} \simeq 6.4$ Å. What this means is that active feedback must be used to damp out the thermal fluctuation of the of the cantilever so that it is less than the spacing between two neighboring nuclei. Piezoelectric, magnetic, or even laser-induced active feedback (see Chapter 3) may be utilized.

In principle the direct detection of a single nuclear spin is possible with nanomagnets on state-of-the-art cantilevers available today. This idea must be pushed forward with carefully designed experiments utilizing active feedback and subnanometer positioning.

Appendix A

Operating The Set-up

This section of the Dissertation has been written to help people who will inherit the setup from me, so that they know how some of the equipment operates.

A.1 Electromagnet

The operation of the electromagnet is pretty straight forward. Due to the age of the magnet the cooling lines are partially clogged up. This Calcium build up can be hypothetically removed with some sort of strong solvent, but it is also possible for the solvent to fill the remaining tiny opening with Calcium thus blocking the pathway of water completely. Without the flow, the solvent will become useless. That is why I never took a risk to clean up the lines.

Even without full power cooling it is possible to maintain the magnetic field at 1.5 Tesla for six hours without heating up the coils too much. When operating, the operator must make sure that coils are not heating up badly. It is advisable to turn the magnet off once the temperature is 60 C.

Before turning the magnet on one must simply make sure that water line is open and water is flowing. And only then one can start up the magnet by turning

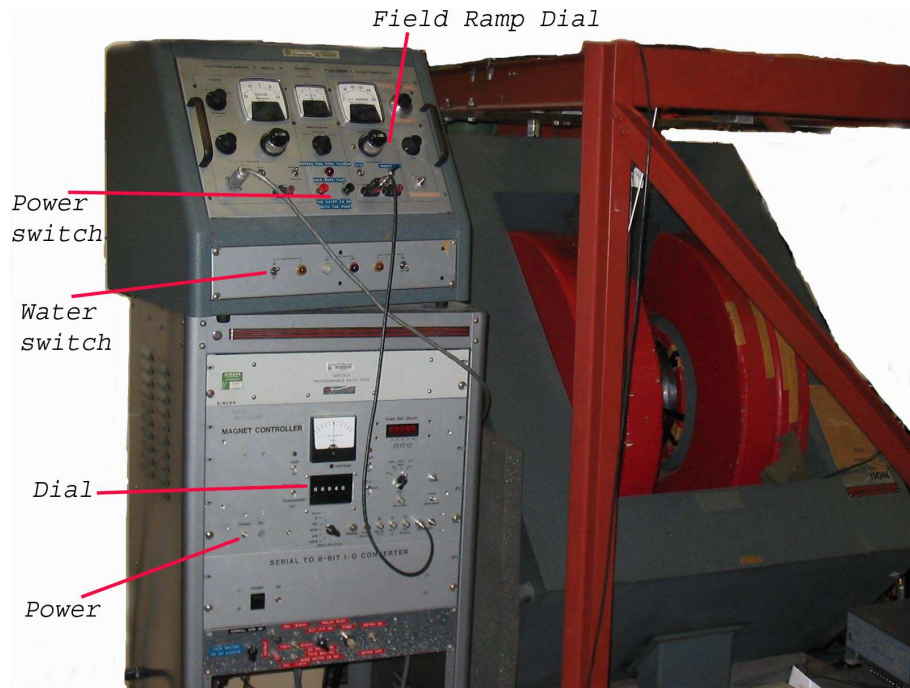


Figure A.1: Electromagnet

the Water switch on. Then one must wait about a minute or so for the electronics to stabilize. After that the "ON" (red) button must be pressed to actually turn the power supply on. It might not work the first time. If this is the case wait 5 seconds and press again. Repeat if necessary. Once the magnet is on, the field can be changed by a home built control unit attached to the Gaussmeter.

The gaussmeter can be turned on before or after the magnet is on, it is not essential for turning the magnet on. To turn on the gaussmeter both the heater and motor switch located directly on the gaussmeter, back of the magnet, must be switched on. The homebuilt control unit must be turned on as well. The sole role of the gaussmeter is to measure the field of the magnet and a home built unit is simply the feedback to the power supply of the magnet that maintains zero difference between the set field field and gaussmeter reading.

The field of the magnet can be changed via the home built unit by simply

changing the dial. The cable going from the output of the home built unit to the external field input of the "Field Feedback Control Unit" of the magnet must be connected so that the home built unit can drive the feedback unit until the desired field value is reached as shown in Figure A.1.

The field also can be ramped up/down by setting the field sweep dial to the desired value. When sweeping the field, the cable connected between the home built unit and the field feedback unit must be disconnected. When operating at constant field mode connect the cable back and set the sweep dial to 0 Gauss/min.

To turn the magnet off, turn the power supply off, and then the water switch. The gaussmeter must be turned off when it is not in use to prevent wear and tear of the bearings.

The "Field Feedback Control Unit" uses batteries for the sweep option and some of the panel displays. These batteries must be replaced in a timely manner (usually every 3 month) for stable performance.

Bibliography

- [1] C. P. Slichter, Principles of Magnetic Resonance (Springer, Berlin, 1996)
- [2] D. Rugar, O. Züger, S. Hoen, C. S. Yannoni, H.-M Vieth, R. D. Kendrick, Science, **264**, 1560 (1994).
- [3] R. Budakian, H. J. Mamin, B. W. Chui, D. Rugar, Science, **307**, 408 (2004).
- [4] D. I. Hoult, R. E. Richards, J. Magn. Reson. **34**, 71(1976).
- [5] J. A. Sidles, D. Rugar, Phys. Rev. Lett., **70**, 3506 (1993)
- [6] N. E. Jenkins, L. P. DeFlores, J. Allen, T. N. Ng, S. R. Garner, S. Kuehn, J. M. Dawlaty, J. A. Marohn, J. Vac. Sci. Technol. B **22**, 909(2004).
- [7] D. Rugar, C. S. Yannoni, J. A. Sidles, Nature, **360**, 563 (1992).
- [8] K. J. Bruland, J. L. Garbini, W. M. Dougherty and J. A. Sidles, J. Appl. Phys. **80**, 1951 (1998).
- [9] J. L. Garbini, K. J. Bruland, W. M. Dougherty and J. A. Sidles, J. Appl. Phys. **83**, 1951 (1996).
- [10] K. J. Bruland, J. L. Garbini, W. M. Dougherty and J. A. Sidles, J. Appl. Phys. **80**, 1959 (1996).

- [11] R. N Kleinamn, G. K. Kaminsky, J. D. Reppy, R. Pindak and D. J. Bishop, Rev. Sci. Instrum. **56**, 2088 (1985).
- [12] B. E. White Jr. and R. O. Pohl, Phys. Rev. Lett. **75**, 4437 (1995).
- [13] K. G. Libbrecht, E. D. Black, C. M. Hirata, Am. J. Phys, **71**, 1208 (2003)
- [14] Model SR830 DSP Lock-In Amplifier, Stanford Research Systems, Sunnyvale, CA (1993)
- [15] D. W. Pohl, Rev. Sci. Instrum., **58**, 54 (1987)
- [16] V. N. Yakimov, Rev Sci. Instrum., **68**, 136 (1997)
- [17] W. R. Silveira and J. A. Marohn, Rev. Sci. Instrum., **74**, 267 (2003)
- [18] Eiichi Fukushima and Stephan B. W. Roeder, Experimental Pulse NMR: A nuts and Bolts Approach (Addison-Wesley Publishing Company, Reading, MA 1981)
- [19] C. W. Miller, Ph.D. thesis, University of Texas at Austin, 2003.
- [20] M. D. Chabot, Ph.D. thesis, University of Texas at Austin, 2001.
- [21] M. Chabot, J. Markert, Proc. SPIE., **4559**, 24-35 (2003).
- [22] M. Chabot, T. Messina, V. Manneevski, C. Miller, J. Markert, Proc. SPIE., **3875**, 104-112 (1999).
- [23] D. Rugar, H. J. Mamin, P. Guethner, Appl. Phys. Lett. **55**, 2588 (1989).
- [24] T. R Albrecht, P. Grutter, D. Rugar, D. P. E. Smith., Ultramicroscopy. **42-44**, 1638 (1992).
- [25] Y. J. Rao, B. Culshaw, Electron. Lett., **27**, 1697 (1991).

- [26] K. Kim, S. Lee., J. Appl. Phys. **91**, 4715 (2002).
- [27] C. H. Metzger and Kh. Karrai et al., Nature, **432**, 1002 (2004).
- [28] G. C. Ratcliff, D. A. Errie, R. Superfine, Appl. Phys. Lett. **72**, 1911 (1998).
- [29] B. Ilic, S Krylov, K Aubin, R. Reichenbach, H.G. Craighead, Appl. Phys. Lett. **86**, 193114 (2005).
- [30] E. U. Condon, H. Odishaw, M. Tortonese, Handbook of Physics (McGraw-Hill Book Co., New York, 1958), p. 5-71
- [31] C. W. Miller and J. T. Markert, *In press* : Phys. Rev. B
- [32] B. C. Stipe, H. J. Mamin, T. D. Stowe, T. W. Kenny, D. Rugar, Phys. Rev. Lett., **86**, 2874, 2001
- [33] J. A. Marohn, R. Fainchtein, D. D. Smith, Appl. Phys. Lett. **73**, 3778 (1998).
- [34] C. W. Miller, U. M. Mirsaidov, T. C. Messina, Y. J. Lee and J. T. Markert, J. Appl. Phys. **93**, 6573 (2003).
- [35] S.R. Kasturi and P.R. Moran, Phys. Rev. B. **12**, 1874 (1975).
- [36] J. A. Ripmeester and N. S. Dalal, Phys. Rev. B. **18**, 3739 (1978).
- [37] S Sun et al., Science. **287**, 1989 (2000).
- [38] S. Rusponi et al., Nature Mater. **2**, 546 (2003).
- [39] P. Gambardella et al., Nature. **416**, 301 (2002)., P. Gambardella et al., Phys. Rev. Lett. **93**, 077203 (2004).
- [40] P. Gambardella et al., Science. **300**, 1130 (2003).
- [41] P. Pouloupoulos et al., Phys. Rev. B. **65**, 064431 (2002).

- [42] J.P. Pierce et al., Phys. Rev. Lett. **92**, 237201 (2004).
- [43] V. Skumryev et al., Nature. **423**, 850 (2002).
- [44] J. Jia et al., Appl. Phys. Lett. **92**, 237201 (2004).
- [45] J. Li et al., Phys. Rev. Lett. **88**, 066101 (2002).
- [46] Ming-Hu Pan et al., Nano Lett. **5**, 87 (2005).
- [47] T. Koide et al., Phys. Rev. Lett. **87**, 257201 (2001).
- [48] C. L. Wooten et al., Phys. Rev. B. **49**, 10023 (2004).
- [49] D. Craik, Magnetism: Principles and Applications, (Wiley, New York, 1995).
- [50] I. Billas et al., Science. **265**, 1682 (1994).
- [51] J. P. Bucher et al., Phys. Rev. Lett. **87**, 3052 (1991).
- [52] C.S. Tian et al., Phys. Rev. Lett. **94**, 137210 (2005).

Vita

Utkur Mirziyodovich Mirsaidov was born January 20, 1980 in Tashkent, Uzbekistan. In 1993 he started attending Uzbek-Turkish Lyceum set up by the initiative of the two governments. He started his undergraduate degree in physics at Tashkent State University in 1995. In 1997 he won the scholarship offered by the government of Uzbekistan and was awarded the opportunity to study at UT-Austin. In his senior year he joined the Markert Group. After completeng his undergraduate degree he decided to stay in Texas as a graduate student and continue to work with John Markert.

Permanent Address: Pushkin Street, 83/27, Tashkent, Uzbekistan 700000

This dissertation was typeset with $\text{\LaTeX} 2_{\epsilon}$ by the author.